

Submitted to: Journal of the Acoustical Society of America

Acoustic scattering by axisymmetric finite-length bodies: An extension of a 2-dimensional conformal mapping method

D. Benjamin Reeder and Timothy K. Stanton

Department of Applied Ocean Physics and Engineering

Woods Hole Oceanographic Institution Woods Hole, Massachusetts 02548

PACS numbers: 43.30.Ft, 43.20.Fn

A general scattering formulation is presented for predicting the far-field scattered pressure from irregular, axisymmetric, finite-length bodies for three boundary conditions—soft, rigid and fluid. The formulation is an extension of a two-dimensional conformal mapping approach [D. T. DiPerna and T. K. Stanton, *J. Acoust. Soc. Am.* 96: 3064-3079 (1994)] to scattering by finite-length bodies. This extended formulation, which is inherently numerically efficient to evaluate, involves conformally mapping the surface of an irregular, finite-length body to a new, orthogonal coordinate system in which the separation of variables method may be used to solve the Helmholtz equation and satisfy the boundary conditions. Extensive comparisons with previously published results using other formulations are presented. This formulation is shown to be very accurate in the prediction of scattering from smooth, symmetric bodies for a wide range of frequencies (Rayleigh through geometric scattering region), scattering angles (monostatic and bistatic), aspect ratios, and for each of the three boundary conditions listed above. Reasonable agreement has also been demonstrated for irregular, realistic shapes with soft boundary conditions.

DISTRIBUTION STATEMENT A
Approved for Public Release
Distribution Unlimited

I. INTRODUCTION

The prediction of acoustic scattering from finite and infinitely long bodies has been pursued for many years, starting with Lord Rayleigh's work on scattering from a sphere (Rayleigh, 1945). Exact analytical solutions to the acoustic wave equation require the scatterer's surface to exactly match the locus of all points for which the radial coordinate is a constant. Such exact analytical solutions exist only for a limited number of cases for which the separation of variables is possible (Morse and Feshbach, 1953; Bowman *et al.*, 1987). In all of these cases, the boundary is simple; e.g., a sphere, infinitely long cylinder and prolate spheroid.

For complex shapes, approximate analytical solutions, including the perturbation method, and approximate asymptotic formulations, such as physical optics (Gaunaurd, 1985) and the geometric theory of diffraction (Levy and Keller, 1959; Yamashita, 1990) have been developed. Numerical solutions have also been developed, including the boundary element method (Tobacman, 1984; Francis, 1993), T-matrix (Waterman, 1968; Varadan *et al.*, 1982; Lakhtakia *et al.*, 1984; Hackman and Todoroff, 1985) and the mode matching methods (Yamashita, 1990). All of these approaches are limited in one or more of the following: frequency range, class of surfaces, types of boundary conditions, eccentricity of shape and/or computational implementation and numerical efficiency.

DiPerna and Stanton (1994) introduced a conformal mapping approach to predicting far-field sound scattering by infinitely long cylinders of noncircular cross section. The approach, termed the Fourier Matching Method (FMM), involves a conformal mapping of variables to a new coordinate system in which the constant radial coordinate exactly matches the scatterer surface. The method makes use of the Newton-Raphson algorithm to execute the mapping.

The boundary conditions are satisfied by requiring the Fourier coefficients in the new angular variable of the total field to be zero, and then the resultant scattered field is expressed in terms of circular eigenfunctions.

The FMM proved to be accurate over a wide range of frequencies, shapes of cross section, and penetrable (fluid) as well as impenetrable boundary conditions. Furthermore, the approach is inherently numerically efficient due to the nature of its formulation. For example, the FMM was shown by DiPerna and Stanton (1994) to be more efficient than the T-matrix method for the case of the high-aspect-ratio elliptic cylinder because fewer terms were needed for the numerical integrations. Even after incorporating the FMM basis functions into the T-matrix calculations, the FMM required 85% fewer integration points.

A major limitation of the two-dimensional FMM was the fact that it was formulated for the case of an infinitely long cylinder—a two-dimensional scattering solution. Many practical scattering problems involve scattering from finite bodies and cannot be accurately modeled by the two-dimensional solution. In order to address this need, the FMM is extended in this paper to predict the scattering from finite-length bodies. In order for this particular approach to be used for finite bodies, the outer boundary of the bodies must be described by a function rotated about the length-wise axis. Hence, although the function is arbitrary and these bodies are three-dimensional, they are restricted to axisymmetric shapes. As with the two-dimensional formulation, this approach is intrinsically numerically efficient and is valid over a wide range of frequencies and shapes as well as both monostatic and bistatic scattering geometries. The extension has been formulated for three boundary conditions—Dirichlet (soft, or pressure-release), Neumann (rigid) and Cauchy (fluid). In all three cases, the surrounding material is fluid.

In Section II, the theoretical basis for the formulation is presented, which includes the development of the new orthogonal coordinate system to which the body is mapped, the conformal mapping procedure, modal series solutions to the transformed Helmholtz equation, and resulting equations for the modal series coefficients after satisfying the three boundary conditions. In Section III, a description of the numerical implementation of the FMM is presented, as well as several practical numerical issues that arise in the solution of the scattering problem. In Section IV, the numerical results are presented for various shapes (spheres, smooth prolate spheroids and two finite bodies with irregular surfaces), boundary conditions (soft, rigid and fluid), and over a wide range of frequencies and scattering angles. The results are compared with various previously published results using other approaches. Section V contains a summary and concluding remarks.

II. THEORY

The derivation of the extended formulation for scattering by an axisymmetric finite-length body is conceptually very similar to the corresponding derivation of the two-dimensional solution described by DiPerna and Stanton (1994); in fact, some of the elements are identical. Both solutions begin with the wave equation in a known coordinate system and conformally map the coordinate variables to a new, orthogonal coordinate system in which the locus of all points where the new radial coordinate is a constant exactly coincides with the scatterer surface. The difference in the coordinate systems between the two cases concerns the fact that one involves two-dimensional coordinates while the other involves an additional coordinate dimension with a new geometry defined for the finite body. Both solutions use mapping functions that are identical in form, transform the Helmholtz equation to the new coordinate system, and satisfy

the boundary conditions using identical techniques to arrive at differing, yet structurally similar, expressions for the scattered pressure. The two-dimensional solution includes a mapping function that corresponds to the shape of the boundary of a cross-sectional slice of the cylinder, while the three-dimensional solution uses a mapping function that corresponds to the shape of the boundary of a *length-wise* slice of the body (specifically, the function that is rotated about the longitudinal axis). Furthermore, the two-dimensional solution includes circular eigenfunctions while the three-dimensional solution for the scattered pressure is expressed in terms of spherical wave functions; i.e., spherical Bessel and Hankel functions and associated Legendre functions. Due to these similarities, the original work will be referred to quite regularly in the development that follows.

Consider the scalar wave equation:

$$\nabla^2 P = \frac{1}{c^2} \frac{\partial^2 P}{\partial t^2}, \quad (1)$$

where P is the acoustic pressure in three dimensions, ∇^2 is the Laplacian operator, c is the speed of sound, and t is time. Assuming a harmonic time dependence, $e^{-i\omega t}$, where ω is the angular frequency, the wave equation becomes the scalar Helmholtz differential equation in Cartesian coordinates:

$$\nabla^2 P(x, y, z) + k^2 P(x, y, z) = 0. \quad (2)$$

Here, $k = \omega/c = 2\pi/\lambda$ is the spatially independent acoustic wave number, and λ is the acoustic wavelength. In all cases considered here, the body does not support shear waves and is surrounded by a fluid medium. By a conformal (angle- and orientation-preserving) transformation

of coordinates, the transformed Helmholtz equation in the new coordinate system becomes:

$$\nabla^2 P(u, w, v) + k^2 F(u, w) P(u, w, v) = 0, \quad (3)$$

where (u, w, v) are the new coordinates, and $F(u, w)$ is a function which depends on the specific transformation (Morse and Feshbach, 1953; DiPerna and Stanton, 1994). With the exception that the wave number is now a function of position, the new Helmholtz equation is formally identical to the Helmholtz equation in Cartesian coordinates.

A. Conformal mapping

Since x , y and z are mutually orthogonal in the Cartesian coordinate system, conformally mapping them into a new coordinate system guarantees that the new coordinates (u, w, v) will be mutually orthogonal, which eases the computation of the normal particle velocity on the boundary. Additionally, the conformal mapping generates a new set of angular functions which fit the scatterer surface more naturally; that is, points along the surface that change rapidly in (x, y, z) are sampled at a higher spatial rate yet are equally spaced in (u, w, v) . A new coordinate system must first be established, and then the conformal mapping function is defined and expanded to provide a method by which the body may be mapped to the new coordinate system.

1. Orthogonal Coordinate System

An orthogonal coordinate system can be generated for a three-dimensional body of revolution from a two-dimensional conformal mapping. Consider the geometry in Fig. 1, in which ϕ is the azimuthal angular coordinate ranging from 0 to 2π (measured from the positive x -axis in the

xy -plane), θ is the polar angular coordinate ranging from 0 to π (measured from the positive z -axis), and r is the radial coordinate ranging from 0 to ∞ . This body is one of revolution that is formed by rotating the contour of the body about the z axis, in the same way that the prolate spheroidal coordinate system is created from an ellipse rotated about the major axis (Flammer, 1957). Consider a new coordinate system whose azimuthal angular coordinate, v , corresponds to ϕ in the original coordinate system. The new polar angular coordinate, w , is measured from the polar axis, z , and ranges from 0 to π , as does the original polar angular coordinate, θ . The scatterer surface in the original coordinate system is defined by the vector, \vec{r} , but in the new coordinate system the scatterer surface is defined by the locus of all points where the new radial coordinate is a constant; specifically, $u = 0$. Defining the functions, $f(u, w)$ and $g(u, w)$, of the new coordinate system as shown in Fig. 1, trigonometry prescribes dimensions of the body in the x , y and z directions to be:

$$x(u, w, v) = f(u, w) \cos(v) \quad (4)$$

$$y(u, w, v) = f(u, w) \sin(v) \quad (5)$$

$$z(u, w, v) = g(u, w). \quad (6)$$

The position vector, \vec{r} , is defined in the new coordinate system by:

$$\vec{r}(u, w, v) = x(u, w, v)\hat{i} + y(u, w, v)\hat{j} + z(u, w, v)\hat{k}, \quad (7)$$

where \hat{i} , \hat{j} , and \hat{k} are unit vectors along the coordinate axes. The position vector can be alternatively expressed by substituting Eqs. (4)-(6) into Eq. (7):

$$\vec{r} = f(u, w) \cos(v) \hat{i} + f(u, w) \sin(v) \hat{j} + g(u, w) \hat{k}. \quad (8)$$

The local projection of \vec{r} in each of the coordinate directions is given by the partial derivative of \vec{r} with respect to each of the variables:

$$\vec{r}_u = f_u(u, w) \cos(v) \hat{i} + f_u(u, w) \sin(v) \hat{j} + g_u(u, w) \hat{k} \quad (9)$$

$$\vec{r}_w = f_w(u, w) \cos(v) \hat{i} + f_w(u, w) \sin(v) \hat{j} + g_w(u, w) \hat{k} \quad (10)$$

$$\vec{r}_v = -f(u, w) \sin(v) \hat{i} + f(u, w) \cos(v) \hat{j}, \quad (11)$$

where the subscript denotes the variable with respect to which the partial derivative is taken.

As mentioned earlier, an orthogonal coordinate system is desirable since it facilitates the computation of the normal particle velocity on the boundary necessary for satisfying the boundary conditions. An orthogonal coordinate system requires the following condition to be satisfied:

$$\vec{r}_u \cdot \vec{r}_v = 0 \quad (12)$$

$$\vec{r}_w \cdot \vec{r}_v = 0 \quad (13)$$

$$\vec{r}_u \cdot \vec{r}_w = 0, \quad (14)$$

which can be expanded as:

$$f_u(u, w)f(u, w)\cos(v)\sin(v)(-1 + 1) = 0 \quad (15)$$

$$f_w(u, w)f(u, w)\cos(v)\sin(v)(-1 + 1) = 0 \quad (16)$$

$$f_u(u, w)f_w(u, w)(\cos^2(v) + \sin^2(v)) + g_u(u, w)g_w(u, w) = 0. \quad (17)$$

The first two conditions are automatically satisfied. The third condition simplifies to:

$$f_u(u, w)f_w(u, w) + g_u(u, w)g_w(u, w) = 0, \quad (18)$$

which will be satisfied if:

$$f_u(u, w) = g_w(u, w) \quad (19)$$

and

$$f_w(u, w) = -g_u(u, w). \quad (20)$$

These are precisely the Cauchy-Riemann equations for an analytic function (Hildebrand, 1964). Therefore, if $f(u, v)$ and $g(u, v)$ are chosen to be harmonic, then the Cauchy-Riemann conditions will be satisfied, making them analytic functions which represent a conformal transformation. A shape initially plotted in the (x, y, z) coordinate system will be transformed into a shape in the (u, w, v) coordinate system with changes in position and size while preserving angles and proportions (Morse and Feshbach, 1953). Orthogonality of the coordinate system as well as the form of the Helmholtz equation will be preserved (Strang, 1986).

2. Mapping Function

As discussed above, a conformal mapping function must be developed to map the scatterer from the old coordinate system to the new orthogonal, axisymmetric coordinate system just developed. It must be noted at this point that, to the authors' knowledge, a general three-dimensional mapping does not exist in the field of mathematics. Due to the fact that conformal mappings are currently limited to two dimensions, the geometry for the finite body must be axisymmetric about one of the axes. The particular mapping used herein is a two-dimensional mapping developed by DiPerna and Stanton (1994) extended to a finite body of revolution which is axisymmetric about the longitudinal axis. The infinitely long cylindrical geometry in DiPerna and Stanton (1994) was described in circular cylindrical coordinates with the radial coordinate, r , being a function of θ , the azimuthal angular coordinate ranging from 0 to 2π . The conformal mapping in that case applied to the function, $r(\theta)$, which corresponded to the shape of the boundary of a cross-sectional slice. In this work, θ is now the *polar* angular coordinate ranging from 0 to π , and ϕ is the azimuthal angular coordinate ranging from 0 to 2π . The function, $r(\theta)$, and associated conformal mapping is now associated with the shape of the boundary of a *length-wise* slice.

The category of surfaces described by Eqs. (4)-(6) has the additional limitation that r be single-valued; i.e., there can be only one value of r for each w . Following DiPerna and Stanton (1994), the mapping procedure for the axisymmetric finite body is commenced by expanding r in a Fourier series relative to the polar angle, θ , shown in Fig. 1:

$$r(\theta) = a + \sum_{n=1}^{\infty} [r_n^c \cos(n\theta) + r_n^s \sin(n\theta)], \quad (21)$$

where a is the average radius of the body, and r_n^c and r_n^s are the usual Fourier series coefficients that in this case correspond to the deviation of the surface from the shape of a circle. Note that the series requires more terms to converge for a high aspect ratio (ratio of length to width) prolate spheroid compared to the Fourier series for a shape that varies little from the shape of a circle. Rewriting the $\cos(n\theta)$ and $\sin(n\theta)$ functions in terms of exponentials and using the expression:

$$R_n \equiv \frac{1}{2}[r_n^c + ir_n^s], \quad (22)$$

gives

$$|r| = ae^{i\theta} + \sum_{n=1}^{\infty} [R_n^* e^{i(1+n)\theta} + R_n e^{i(1-n)\theta}]. \quad (23)$$

For a conformal mapping from the (x, y, z) coordinate system to the new coordinate system in (u, w, v) :

$$M(\rho) = M(u + iw), \quad (24)$$

where $M(\rho)$ is the analytic mapping function in terms of u , the radial variable, and w , the polar angular variable, and $\rho \equiv u + iw$. It is desirable to make scattering predictions using this model without inversely mapping the results of this model back to the original coordinate system. The potentially difficult inverse mapping is avoided by choosing $M(\rho)$ such that the coordinate system becomes spherical as the radial coordinate is increased. While the choice of such a mapping function allows predictions of this model to be easily compared to existing solutions, it restricts direct comparisons to the far-field only. The general approach can certainly be used in the near-field, but comparisons of near-field scattering between this formulation and other solutions would require an inverse mapping. Note also that there will be two different

mapping functions: $G(\rho)$ for the exterior problem and $T(\rho)$ for the interior problem. For the interior problem, $T(\rho)$ is chosen such that the coordinate system becomes spherical as the radial coordinate is decreased.

For the exterior problem, $G(\rho)$ must be chosen such that:

- (1) As $u \rightarrow \infty$, the coordinate system becomes spherical,
- (2) the transformed Helmholtz equation is solvable, and
- (3) $u = 0$ is the scatterer surface.

The first two conditions can be satisfied by choosing the form of the exterior mapping function (DiPerna and Stanton, 1994) to be:

$$G(\rho) = c_{-1}e^\rho + \sum_{n=0}^{\infty} c_n e^{-n\rho}, \quad (25)$$

which can be decomposed into the complex components:

$$g(u, w) \equiv \operatorname{Re}(G(\rho)) = c_{-1}e^u \cos(w) + \sum_{n=0}^{\infty} c_n e^{-nu} \cos(nw) \quad (26)$$

and

$$f(u, w) \equiv \operatorname{Im}(G(\rho)) = c_{-1}e^u \sin(w) + \sum_{n=0}^{\infty} c_n e^{-nu} \sin(nw). \quad (27)$$

The coefficients of the mapping function must be chosen such that $u = 0$ defines the scatterer surface in the new coordinate system. Equating the functions in Eq. (23) and Eq. (25) (with $u = 0$) that represent the surface in the two coordinate systems gives:

$$ae^{i\theta} + \sum_{n=1}^{\infty} [R_n^* e^{i(1+n)\theta} + R_n e^{i(1-n)\theta}] = c_{-1}e^{iw} + \sum_{n=0}^{\infty} c_n e^{-inw}. \quad (28)$$

Since the left-hand side contains positive and negative frequency components while the right-hand side contains only negative frequency components (with the exception of $c_{-1}e^{iw}$), θ and w are not equal; therefore, it is necessary to determine the extent to which θ depends on w . Since it was assumed earlier that the surface is periodic and can be represented as a Fourier series, the deviation of θ from w will be periodic and can be represented as a Fourier series. Specifically, assume:

$$\theta(w) = w + \sum_{l=1}^{\infty} [\delta_l^c \cos(lw) + \delta_l^s \sin(lw)]. \quad (29)$$

The conformal mapping relies on the choice of δ_l^c and δ_l^s such that Eq. (28) is satisfied. Using the orthogonality relationships of complex exponential functions, multiplying both sides by $(1/2\pi)e^{-ijw}$ and integrating over w from 0 to 2π gives:

$$\frac{1}{2\pi} \int_0^{2\pi} e^{-ijw} \left(ae^{i\theta(w)} + \sum_{n=1}^{\infty} [R_n^* e^{i(1+n)\theta(w)} + R_n e^{i(1-n)\theta(w)}] \right) dw = \begin{cases} 0, & j > 1 \\ c_j, & j \leq 1 \end{cases}, \quad (30)$$

where j is an integer. This set of nonlinear constraints is identical in form to that of DiPerna and Stanton (1994) and is solved by use of an extension of the Newton-Raphson method, the details of which are laid out in Appendix A of DiPerna and Stanton (1994). Note, however, that even though the integral in Eq. (30) is performed from 0 to 2π , w is defined in the scattering geometry from 0 to π only (not 2π). Consequently, the mapping coefficients are computed based on the periodic extension from 0 to 2π , but only half of them are used. The upper result in the right hand side of Eq. (30) is used to solve for the values of δ_l^c and δ_l^s , which are then used to solve for the mapping coefficients, c_n , through use of the lower result in the right hand side of Eq. (30).

The uniqueness of the transformation is tested by verifying that the Jacobian of the transformation is nonzero. This ensures that there exists only one (x, z) for each (u, w) . Specifically:

$$|G'(\rho)|^2 \neq 0, \quad u \geq 0. \quad (31)$$

The interior mapping procedure is identical to the exterior mapping procedure with the exception that the interior mapping function, $T(\rho)$, is different from $G(\rho)$; specifically, $T(\rho)$ is chosen such that the coordinate system becomes spherical as the radial coordinate is decreased. The remaining two conditions mentioned above in the choice of $G(\rho)$ remain the same for the interior problem. These conditions are satisfied by:

$$T(\rho) = \sum_{n=0}^{\infty} t_n e^{n\rho}. \quad (32)$$

To summarize, the procedure described above to conformally map the scatterer shape from the original coordinate system to a new coordinate system is identical in form to the procedure presented in DiPerna and Stanton (1994). In this study, the same mapping procedure is extended to a different (finite-length, axisymmetric) scattering geometry; specifically, it is extended to the shape of the boundary in the length-wise slice. The results of this mapping will be used in solving the Helmholtz equation in three dimensions in the next section.

B. Solutions to the Helmholtz equation

The 3-dimensional Helmholtz equation from Eq. (2) in the original coordinate system is

expressed in spherical coordinates as:

$$\nabla^2 P(r, \theta, \phi) + k^2 P(r, \theta, \phi) = 0, \quad (33)$$

the general solution to which is:

$$\begin{aligned} P^{ext}(r, \theta, \phi) = & \sum_{n=-\infty}^{\infty} \sum_{m=-\infty}^{\infty} a_{nm} j_n(kr) P_n^m(\cos(\theta)) e^{im\phi} \\ & + \sum_{n=-\infty}^{\infty} \sum_{m=-\infty}^{\infty} b_{nm} h_n^{(1)}(kr) P_n^m(\cos(\theta)) e^{im\phi}, \end{aligned} \quad (34)$$

where $j_n(kr)$ is the spherical Bessel function of the first kind of order n , $h_n^{(1)}(kr)$ is the spherical Hankel function of the first kind of order n , and $P_n^m(\cos(\theta))$ is the associated Legendre function of degree n and order m . The radial coordinate is r , the polar angular coordinate is θ , and the azimuthal angular coordinate is ϕ . The scattered field coefficients, b_{nm} , are determined by satisfying the boundary conditions using the known coefficients, a_{nm} , of the incident plane wave field traveling from the θ_0 direction relative to the z -axis:

$$a_{nm} = i^n \epsilon_m (2n+1) \frac{\Gamma(n-m+1)}{\Gamma(n+m+1)} P_n^m(\cos(\theta_0)), \quad (35)$$

where ϵ_m is the Neumann factor, and Γ is the gamma function.

$P^{ext}(r, \theta, \phi)$ is the total pressure external to the scatterer in the original coordinate system (i.e. before transformation): the first term in Eq. (34) represents the incident pressure, and the second term represents the scattered pressure. Quantities in the original coordinate system can

be expressed in terms of the new coordinate system defined in Sec. II.A.1 and Fig. 1:

$$\phi = v \quad (36)$$

$$r(u, w) = \sqrt{f^2(u, w) + g^2(u, w)} \quad (37)$$

$$\cos(\theta(u, w)) = \frac{g(u, w)}{r(u, w)}. \quad (38)$$

Using these relations, the conformal mapping transforms the Helmholtz equation (Eq. (33)) into:

$$\nabla^2 P(u, w, v) + k^2 F(u, w) P(u, w, v) = 0, \quad (39)$$

the solution to which is:

$$\begin{aligned} P^{ext}(u, w, v) = & \sum_{n=-\infty}^{\infty} \sum_{m=-\infty}^{\infty} a_{nm} j_n(kr(u, w)) P_n^m \left(\frac{g(u, w)}{r(u, w)} \right) e^{imv} \\ & + \sum_{n=-\infty}^{\infty} \sum_{m=-\infty}^{\infty} b_{nm} h_n^{(1)}(kr(u, w)) P_n^m \left(\frac{g(u, w)}{r(u, w)} \right) e^{imv}, \end{aligned} \quad (40)$$

which is now the expression for the total far-field pressure in the new coordinate system as the sum of the incident and scattered pressure fields, respectively.

The procedure to determine the pressure field inside the scatterer is identical in nature to the exterior problem, but the mapping function is different for the interior problem; therefore, the new Helmholtz equation is identical in form, but incorporates a different wave number, k_1 , to accurately characterize the material properties of the scatterer's interior. The expression for

the interior pressure field becomes:

$$P^{\text{int}}(u, w, v) = \sum_{n=-\infty}^{\infty} \sum_{m=-\infty}^{\infty} l_{nm} j_n(k_1 r(u, w)) P_n^m \left(\frac{g(u, w)}{r(u, w)} \right) e^{imv}, \quad (41)$$

where l_{nm} are the internal field coefficients. Only the spherical Bessel function is included in the expression for the internal field since the spherical Hankel function becomes infinite at the origin.

In the limit of great distances from the scatterer, the coordinate system becomes spherical, and the asymptotic form of the Hankel function varies inversely with distance. The scattered pressure (the second term in Eq. (40)) in this far-field limit has the form:

$$P^{\text{scat}} \xrightarrow{u \rightarrow \infty} P^{\text{inc}} \frac{e^{ikr}}{r} f_s, \quad (42)$$

where the scattering amplitude, f_s , having units of length, is a measure of the efficiency with which an object scatters sound and is a function of the object's size, shape, orientation, material properties and the wavelength of the incident wave. The scattering amplitude is given in general form as:

$$f_s = \sum_{n=-\infty}^{\infty} \sum_{m=-\infty}^{\infty} b_{nm} i^{-n-1} P_n^m \left(\frac{g(u, w)}{r(u, w)} \right) e^{imv}. \quad (43)$$

The far-field scattered energy evaluated in the backscatter direction is often expressed in terms of the target strength (TS) with units of decibels (dB) relative to 1 m (Urick, 1983), which is given by:

$$TS = 10 \log \sigma_{bs} = 10 \log |f_{bs}|^2, \quad (44)$$

where f_{bs} is the scattering amplitude evaluated in the backscattering direction, and $\sigma_{bs} = |f_{bs}|^2$ is the differential backscattering cross section, which differs from the often-used backscattering cross section, σ , by a factor of 4π ($\sigma = 4\pi\sigma_{bs}$). In order to compare scattering from objects of different sizes but similar proportions, target strength is often normalized by the square of some typical dimension. Using the length (L) of the elongated scatterer as the normalization constant, the “reduced” target strength (RTS) is:

$$RTS = 10 \log \left(\frac{\sigma_{bs}}{L^2} \right) = 10 \log |f_{bs}|^2 - 10 \log(L^2) = 10 \log \left| \frac{f_{bs}}{L} \right|^2. \quad (45)$$

In the case of a sphere, the target strength is normalized by πa^2 instead of L^2 . An alternative expression often used to represent the energy scattered in three dimensions is the normalized, steady-state form function (Neubauer, 1986):

$$f_\infty = \frac{2}{a} f_s, \quad (46)$$

where a is the radius of a sphere or the semi-minor axis of a prolate spheroid.

To summarize, a new orthogonal coordinate system has been established to which the original coordinate system is mapped via a conformal mapping function. The scatterer surface in the new coordinate system is defined by the locus of all points where the radial coordinate is a constant. The solution to the Helmholtz equation in the new coordinate system will have the same form as the original solution, but with new coordinates using the realizations of Eqs. (36) - (38). This can be confirmed by inspecting the case of the exterior field for the spherical scatterer: $r(u, w) = c_{-1} e^u$, $\theta(u, w) = w$ and $\phi = v$, resulting in the same solution as in spherical

coordinates using separation of variables. Also, for the case far ($u \rightarrow \infty$) from the non-spherical scatterer: $r(u, w) \rightarrow c_{-1}e^u$, $\theta(u, w) \rightarrow w$ and $\phi = v$, resulting in the same solution as in spherical coordinates in the far-field. Equations (40) and (41) are a general solution for the total pressure in the case of acoustic scattering from a finite-length, axisymmetric body for all frequencies, all angles (bistatic scattering), and for impenetrable (soft and rigid) and penetrable (fluid) boundary conditions. All the quantities needed to satisfy soft, hard and fluid boundary conditions have now been established. Each boundary condition generates a different set of modal series coefficients, b_{nm} , which are used in Eq. (43) to compute the scattering amplitude. These coefficients will be determined for three boundary conditions in the following section.

C. Boundary conditions

The solution for the scattered field in Eqs. (40) and (43) depends on the boundary conditions. For each boundary condition, there is a different set of scattered field coefficients, b_{nm} , which needs to be evaluated. These coefficients are determined in the normal approach in which the pressures and/or velocities are matched at the boundaries. This matching is specific to the material properties on each side of the boundary. For each of the different boundary conditions, expressions are derived in the following sections for b_{nm} , all of which are in terms of the parameters of the new coordinate system.

The challenge presented by an irregular body is finding a solution to a system of equations in order to satisfy the boundary conditions; specifically, a set of functions, ψ , must be determined by which the basis functions are multiplied to generate the system of equations. For a separable geometry, ψ is chosen to be the angular eigenfunction to yield a closed-form solution based on the orthogonality of the eigenfunctions. In the case of irregular surfaces that do not conform

to coordinate surfaces, a set of functions, ψ , must be chosen to solve the system of equations. DiPerna and Stanton (1994) chose the eigenfunctions in the new (cylindrical) coordinate system, $\psi_m = e^{-imv}$. It is in this choice of eigenfunctions that the FMM derives its name. Without the conformal change of variables to (u, w, v) , this choice of functions would not be possible. For the three-dimensional case, the eigenfunctions in the spherical coordinate system are chosen; specifically (Morse and Feshbach, 1953):

$$\psi_n^m = P_n^m(\cos(w)) \sin(w) e^{-imv}. \quad (47)$$

Using this choice for ψ , a system of equations is generated to satisfy each of the boundary conditions discussed herein (soft, rigid and fluid). The system of equations is solved for the scattered field coefficients, b_{nm} , which are then used in Eq. (43) to determine the scattering amplitude.

1. Dirichlet boundary conditions

For soft (pressure release or Dirichlet) boundary conditions, the total pressure vanishes on the surface of the scatterer; i.e., $P^{\text{ext}}(u_0, w, v) = 0$. Using Eq. (40), the series solution for the total exterior pressure field evaluated at the boundary with pressure release boundary conditions is set equal to zero:

$$\begin{aligned} & \sum_{n=-\infty}^{\infty} \sum_{m=-\infty}^{\infty} a_{nm} j_n(kr(u_0, w)) P_n^m \left(\frac{g(u_0, w)}{r(u_0, w)} \right) e^{imv} \\ & + \sum_{n=-\infty}^{\infty} \sum_{m=-\infty}^{\infty} b_{nm} h_n^{(1)}(kr(u_0, w)) P_n^m \left(\frac{g(u_0, w)}{r(u_0, w)} \right) e^{imv} = 0. \end{aligned} \quad (48)$$

The system of equations necessary to satisfy this boundary condition is generated by multiplying both sides of this equation by ψ_n^m from Eq. (47) and integrating over the range of w and v (Morse and Feshbach, 1953):

$$\begin{aligned} & \int_0^\pi \int_0^{2\pi} \left\{ \left(\sum_{n=-\infty}^{\infty} \sum_{m=-\infty}^{\infty} a_{nm} j_n(kr(u_0, w)) P_n^m \left(\frac{g(u_0, w)}{r(u_0, w)} \right) e^{imv} \right. \right. \\ & \quad \left. \left. + \sum_{n=-\infty}^{\infty} \sum_{m=-\infty}^{\infty} b_{nm} h_n^{(1)}(kr(u_0, w)) P_n^m \left(\frac{g(u_0, w)}{r(u_0, w)} \right) e^{imv} \right) \right. \\ & \quad \left. \times P_n^m(\cos(w)) \sin(w) e^{-imv} \right\} dv dw = 0. \end{aligned} \quad (49)$$

Performing the integration on v gives:

$$\begin{aligned} & \sum_{n=-\infty}^{\infty} a_{nm} \int_0^\pi \left(j_n(kr(u_0, w)) P_n^m \left(\frac{g(u_0, w)}{r(u_0, w)} \right) P_n^m(\cos(w)) \sin(w) \right) dw \\ & \quad + \sum_{n=-\infty}^{\infty} b_{nm} \int_0^\pi \left(h_n^{(1)}(kr(u_0, w)) P_n^m \left(\frac{g(u_0, w)}{r(u_0, w)} \right) P_n^m(\cos(w)) \sin(w) \right) dw = 0, \end{aligned} \quad (50)$$

for each azimuthal order m . This system of equations for pressure release boundary conditions can be written in compact form:

$$\sum_{n=-\infty}^{\infty} a_{nm} R_n^m + \sum_{n=-\infty}^{\infty} b_{nm} Q_n^m = 0, \quad (51)$$

where a_{nm} is given in Eq. (35), and R_n^m and Q_n^m are defined, using Eq. (50), as:

$$R_n^m \equiv \int_0^\pi \left(j_n(kr(u_0, w)) P_n^m \left(\frac{g(u_0, w)}{r(u_0, w)} \right) P_n^m(\cos(w)) \sin(w) \right) dw \quad (52)$$

$$Q_n^m \equiv \int_0^\pi \left(h_n^{(1)}(kr(u_0, w)) P_n^m \left(\frac{g(u_0, w)}{r(u_0, w)} \right) P_n^m(\cos(w)) \sin(w) \right) dw. \quad (53)$$

Using Eq. (51), the series coefficients, b_{nm} , for the scattered field due to a soft boundary are:

$$b_{nm} = - (Q_n^m)^{-1} R_n^m a_{nm}, \quad (54)$$

where $(\dots)^{-1}$ denotes a matrix inversion.

2. Neumann boundary conditions

With rigid, or Neumann, boundary conditions, the normal particle velocity vanishes on the scatterer surface; i.e., $\hat{n} \cdot \nabla P^{\text{ext}}(u_0, w, v) = 0$, where \hat{n} is the unit vector normal to the surface, and ∇ is the gradient operator. The method to solve for b_{nm} is broadly similar to the previous case, although several new terms are necessary to satisfy this particular boundary condition.

The unit vectors in the u , v , and w directions are (Hildebrand, 1964):

$$\hat{a}_u = \frac{\vec{r}_u}{|\vec{r}_u|} \quad (55)$$

$$\hat{a}_w = \frac{\vec{r}_w}{|\vec{r}_w|} \quad (56)$$

$$\hat{a}_v = \frac{\vec{r}_v}{|\vec{r}_v|}. \quad (57)$$

Using Eqs. (9) - (11), the scale factors of each of the new coordinates (Morse and Feshbach, 1953) can be rewritten using the new coordinates:

$$h_u = |\vec{r}_u| = \sqrt{f_u^2(u, w) + g_u^2(u, w)} = \sqrt{f_u^2(u, w) + f_w^2(u, w)} \quad (58)$$

$$h_w = |\vec{r}_w| = \sqrt{f_w^2(u, w) + g_w^2(u, w)} = \sqrt{f_w^2(u, w) + f_u^2(u, w)} \quad (59)$$

$$h_v = |\vec{r}_v| = f(u, w). \quad (60)$$

Note that:

$$h_u(u, w) = h_w(u, w) = h(u, w). \quad (61)$$

In the new coordinate system, the unit vectors become:

$$\hat{a}_u = \frac{f_u(u, w)}{h(u, w)} \cos(v) \hat{i} + \frac{f_u(u, w)}{h(u, w)} \sin(v) \hat{j} + \frac{g_u(u, w)}{h(u, w)} \hat{k} \quad (62)$$

$$\hat{a}_w = \frac{f_w(u, w)}{h(u, w)} \cos(v) \hat{i} + \frac{f_w(u, w)}{h(u, w)} \sin(v) \hat{j} + \frac{g_w(u, w)}{h(u, w)} \hat{k} \quad (63)$$

$$\hat{a}_v = -\sin(v) \hat{i} + \cos(v) \hat{j}. \quad (64)$$

The scatterer surface has been defined by $u = u_0$; therefore, $\hat{n} = \hat{a}_u$. The gradient of P is:

$$\nabla P(u, w, v) = \frac{1}{h_u(u, w)} \frac{\partial P}{\partial u} \hat{a}_u + \frac{1}{h_w(u, w)} \frac{\partial P}{\partial w} \hat{a}_w + \frac{1}{h_v(u, w)} \frac{\partial P}{\partial v} \hat{a}_v. \quad (65)$$

Using $\hat{n} = \hat{a}_u$ and $h_u(u, w) = \sqrt{f_w^2(u, w) + f_u^2(u, w)}$:

$$\hat{n} \cdot \nabla P(u, w, v) = \frac{1}{\sqrt{f_w^2(u, w) + f_u^2(u, w)}} \frac{\partial P}{\partial u}. \quad (66)$$

Using Eq. (40), the series solution for the normal particle velocity of the total external field

for rigid boundary conditions evaluated at the boundary is set equal to zero:

$$\begin{aligned} & \hat{n} \cdot \nabla \left(\sum_{n=-\infty}^{\infty} \sum_{m=-\infty}^{\infty} a_{nm} j_n(kr(u_0, w)) P_n^m \left(\frac{g(u_0, w)}{r(u_0, w)} \right) e^{imv} \right) \\ & + \hat{n} \cdot \nabla \left(\sum_{n=-\infty}^{\infty} \sum_{m=-\infty}^{\infty} b_{nm} h_n^{(1)}(kr(u_0, w)) P_n^m \left(\frac{g(u_0, w)}{r(u_0, w)} \right) e^{imv} \right) = 0. \end{aligned} \quad (67)$$

The system of equations necessary to satisfy this boundary condition is generated by multiplying both sides of the equation by ψ_n^m in Eq (47) and integrating over the range of w and v :

$$\begin{aligned} & \int_0^\pi \int_0^{2\pi} \left\{ \left(\hat{n} \cdot \nabla \left(\sum_{n=-\infty}^{\infty} \sum_{m=-\infty}^{\infty} a_{nm} j_n(kr(u_0, w)) P_n^m \left(\frac{g(u_0, w)}{r(u_0, w)} \right) e^{imv} \right) \right. \right. \\ & \left. \left. + \hat{n} \cdot \nabla \left(\sum_{n=-\infty}^{\infty} \sum_{m=-\infty}^{\infty} b_{nm} h_n^{(1)}(kr(u_0, w)) P_n^m \left(\frac{g(u_0, w)}{r(u_0, w)} \right) e^{imv} \right) \right) \right\} \\ & \times P_n^m(\cos(w)) \sin(w) e^{-imv} dv dw = 0. \end{aligned} \quad (68)$$

Using Eq. (66) and performing the integration on v gives:

$$\begin{aligned} & \sum_{n=-\infty}^{\infty} a_{nm} \int_0^\pi \left(j_n(kr(u_0, w)) P_{n,u}^m \left(\frac{g(u_0, w)}{r(u_0, w)} \right) \frac{r(u_0, w) g_u(u_0, w) - g(u_0, w) r_u(u_0, w)}{r^2(u_0, w)} \right. \\ & \left. + j_{n,u}(kr(u_0, w)) P_n^m \left(\frac{g(u_0, w)}{r(u_0, w)} \right) k r_u(u_0, w) \right) \frac{P_n^m(\cos(w))}{\sqrt{f_w^2(u_0, w) + f_u^2(u_0, w)}} \sin(w) dw \\ & + \sum_{n=-\infty}^{\infty} b_{nm} \int_0^\pi \left(h_n^{(1)}(kr(u_0, w)) P_{n,u}^m \left(\frac{g(u_0, w)}{r(u_0, w)} \right) \frac{r(u_0, w) g_u(u_0, w) - g(u_0, w) r_u(u_0, w)}{r^2(u_0, w)} \right. \\ & \left. + h_{n,u}^{(1)}(kr(u_0, w)) P_n^m \left(\frac{g(u_0, w)}{r(u_0, w)} \right) k r_u(u_0, w) \right) \frac{P_n^m(\cos(w))}{\sqrt{f_w^2(u_0, w) + f_u^2(u_0, w)}} \sin(w) dw = 0, \end{aligned} \quad (69)$$

where, as with the other terms, the subscript, u , also indicates the partial derivative of the Legendre functions with respect to u .

As in the previous section, the system of equations for rigid boundary conditions can be written in compact form:

$$\sum_{n=-\infty}^{\infty} a_{nm} R_n'^m + \sum_{n=-\infty}^{\infty} b_{nm} Q_n'^m = 0, \quad (70)$$

where a_{nm} is given in Eq. (35), $R_n'^m$ is the integral in the first half of Eq. (69), and $Q_n'^m$ is the integral in the second half of Eq. (69). Using Eq. (70), the series coefficients, b_{nm} , for the far-field scattered field due to a rigid boundary are:

$$b_{nm} = - (Q_n'^m)^{-1} R_n'^m a_{nm}. \quad (71)$$

3. Cauchy boundary conditions

Fluid (Cauchy) boundary conditions is the case in which the body consists of a fluid with material properties other than that of the surrounding fluid and does not support a shear wave. In this case, the exterior and interior pressure fields and normal components of particle velocity are required to be equal on the surface. The fluid boundary conditions take the form:

Pressure:

$$\begin{aligned} & \sum_{n=-\infty}^{\infty} \sum_{m=-\infty}^{\infty} a_{nm} j_n(kr(u_0, w)) P_n^m \left(\frac{g(u_0, w)}{r(u_0, w)} \right) e^{imv} \\ & + \sum_{n=-\infty}^{\infty} \sum_{m=-\infty}^{\infty} b_{nm} h_n^{(1)}(kr(u_0, w)) P_n^m \left(\frac{g(u_0, w)}{r(u_0, w)} \right) e^{imv} \\ & = \sum_{n=-\infty}^{\infty} \sum_{m=-\infty}^{\infty} l_{nm} j_n(k_1 r(u_0, w)) P_n^m \left(\frac{g(u_0, w)}{r(u_0, w)} \right) e^{imv} \end{aligned} \quad (72)$$

Particle Velocity:

$$\begin{aligned}
& \hat{n} \cdot \nabla \left(\sum_{n=-\infty}^{\infty} \sum_{m=-\infty}^{\infty} a_{nm} j_n(kr(u_0, w)) P_n^m \left(\frac{g(u_0, w)}{r(u_0, w)} \right) e^{imv} \right) \\
& + \hat{n} \cdot \nabla \left(\sum_{n=-\infty}^{\infty} \sum_{m=-\infty}^{\infty} b_{nm} h_n^{(1)}(kr(u_0, w)) P_n^m \left(\frac{g(u_0, w)}{r(u_0, w)} \right) e^{imv} \right) \\
& = \hat{n} \cdot \nabla \left(\sum_{n=-\infty}^{\infty} \sum_{m=-\infty}^{\infty} l_{nm} j_n(k_1 r(u_0, w)) P_n^m \left(\frac{g(u_0, w)}{r(u_0, w)} \right) e^{imv} \right), \tag{73}
\end{aligned}$$

where l_{nm} are the interior field coefficients. The system of equations necessary to satisfy this boundary condition is generated by multiplying both sides of the equation by ψ_n^m in Eq (47) and integrating over the range of w and v :

Pressure:

$$\begin{aligned}
& \int_0^\pi \int_0^{2\pi} \left\{ \left(\sum_{n=-\infty}^{\infty} \sum_{m=-\infty}^{\infty} a_{nm} j_n(kr(u_0, w)) P_n^m \left(\frac{g(u_0, w)}{r(u_0, w)} \right) e^{imv} \right. \right. \\
& \left. \left. + \sum_{n=-\infty}^{\infty} \sum_{m=-\infty}^{\infty} b_{nm} h_n^{(1)}(kr(u_0, w)) P_n^m \left(\frac{g(u_0, w)}{r(u_0, w)} \right) e^{imv} \right) \right. \\
& \left. \times P_n^m(\cos(w)) \sin(w) e^{-imv} \right\} dv dw \\
& = \int_0^\pi \int_0^{2\pi} \left\{ \left(\sum_{n=-\infty}^{\infty} \sum_{m=-\infty}^{\infty} l_{nm} j_n(k_1 r(u_0, w)) P_n^m \left(\frac{g(u_0, w)}{r(u_0, w)} \right) e^{imv} \right) \right. \\
& \left. \times P_n^m(\cos(w)) \sin(w) e^{-imv} \right\} dv dw \tag{74}
\end{aligned}$$

Particle Velocity:

$$\begin{aligned}
& \int_0^\pi \int_0^{2\pi} \left\{ \left(\hat{n} \cdot \nabla \left(\sum_{n=-\infty}^{\infty} \sum_{m=-\infty}^{\infty} a_{nm} j_n(kr(u_0, w)) P_n^m \left(\frac{g(u_0, w)}{r(u_0, w)} \right) e^{imv} \right) \right. \right. \\
& \quad \left. \left. + \hat{n} \cdot \nabla \left(\sum_{n=-\infty}^{\infty} \sum_{m=-\infty}^{\infty} b_{nm} h_n^{(1)}(kr(u_0, w)) P_n^m \left(\frac{g(u_0, w)}{r(u_0, w)} \right) e^{imv} \right) \right) \right. \\
& \quad \times P_n^m(\cos(w)) \sin(w) e^{-imv} \} dv dw \\
& = \int_0^\pi \int_0^{2\pi} \left\{ \hat{n} \cdot \nabla \left(\sum_{n=-\infty}^{\infty} \sum_{m=-\infty}^{\infty} l_{nm} j_n(k_1 r(u_0, w)) P_n^m \left(\frac{g(u_0, w)}{r(u_0, w)} \right) e^{imv} \right) \right. \\
& \quad \times P_n^m(\cos(w)) \sin(w) e^{-imv} \} dv dw.
\end{aligned} \tag{75}$$

Using Eq. (66) and performing the integration on v for both Eqs. (74) and (75) gives:

Pressure:

$$\begin{aligned}
& \sum_{n=-\infty}^{\infty} a_{nm} \int_0^\pi j_n(kr(u_0, w)) P_n^m \left(\frac{g(u_0, w)}{r(u_0, w)} \right) P_n^m(\cos(w)) \sin(w) dw \\
& + \sum_{n=-\infty}^{\infty} b_{nm} \int_0^\pi h_n^{(1)}(kr(u_0, w)) P_n^m \left(\frac{g(u_0, w)}{r(u_0, w)} \right) P_n^m(\cos(w)) \sin(w) dw \\
& = \sum_{n=-\infty}^{\infty} l_{nm} \int_0^\pi j_n(k_1 r(u_0, w)) P_n^m \left(\frac{g(u_0, w)}{r(u_0, w)} \right) P_n^m(\cos(w)) \sin(w) dw
\end{aligned} \tag{76}$$

Particle Velocity:

$$\begin{aligned}
& \sum_{n=-\infty}^{\infty} a_{nm} \int_0^{\pi} \left(j_n(kr(u_0, w)) P_n^m \left(\frac{g(u_0, w)}{r(u_0, w)} \right) \frac{r(u_0, w)g_u(u_0, w) - g(u_0, w)r_u(u_0, w)}{r^2(u_0, w)} \right. \\
& \quad \left. + j_{n,u}(kr(u_0, w)) P_n^m \left(\frac{g(u_0, w)}{r(u_0, w)} \right) kr_u(u_0, w) \right) \frac{P_n^m(\cos(w))}{\sqrt{f_w^2(u_0, w) + f_u^2(u_0, w)}} \sin(w) dw \\
& + \sum_{n=-\infty}^{\infty} b_{nm} \int_0^{\pi} \left(h_n^{(1)}(kr(u_0, w)) P_n^m \left(\frac{g(u_0, w)}{r(u_0, w)} \right) \frac{r(u_0, w)g_u(u_0, w) - g(u_0, w)r_u(u_0, w)}{r^2(u_0, w)} \right. \\
& \quad \left. + h_{n,u}^{(1)}(kr(u_0, w)) P_n^m \left(\frac{g(u_0, w)}{r(u_0, w)} \right) kr_u(u_0, w) \right) \frac{P_n^m(\cos(w))}{\sqrt{f_w^2(u_0, w) + f_u^2(u_0, w)}} \sin(w) dw \quad (77) \\
& = \sum_{n=-\infty}^{\infty} l_{nm} \int_0^{\pi} \left(j_n(k_1 r(u_0, w)) P_n^m \left(\frac{g(u_0, w)}{r(u_0, w)} \right) \frac{r(u_0, w)g_u(u_0, w) - g(u_0, w)r_u(u_0, w)}{r^2(u_0, w)} \right. \\
& \quad \left. + j_{n,u}(k_1 r(u_0, w)) P_n^m \left(\frac{g(u_0, w)}{r(u_0, w)} \right) k_1 r_u(u_0, w) \right) \frac{P_n^m(\cos(w))}{\sqrt{f_w^2(u_0, w) + f_u^2(u_0, w)}} \sin(w) dw.
\end{aligned}$$

Writing Eqs. (76) and (77) in compact form:

$$\sum_{n=-\infty}^{\infty} a_{nm} R_n^m + \sum_{n=-\infty}^{\infty} b_{nm} Q_n^m = \sum_{n=-\infty}^{\infty} l_{nm} S_n^m \quad (78)$$

$$\sum_{n=-\infty}^{\infty} a_{nm} R_n'^m + \sum_{n=-\infty}^{\infty} b_{nm} Q_n'^m = \sum_{n=-\infty}^{\infty} l_{nm} S_n'^m, \quad (79)$$

where a_{nm} is given in Eq. (35); R_n^m , Q_n^m and S_n^m are now the first, second and third integrals in Eq. (76); and $R_n'^m$, $Q_n'^m$ and $S_n'^m$ are now the first, second and third integrals in Eq. (77). In contrast to the above two cases of impenetrable boundary conditions, b_{nm} must be solved for in

two simultaneous equations. Solving for b_{nm} in Eqs. (78) and (79):

$$b_{nm} = - (Q_n^{im} S_n^{im} - Q_n^m S_n^{im})^{-1} (R_n^m S_n^{im} - R_n^{im} S_n^m) a_{nm}. \quad (80)$$

In summary, the scattering amplitude (Eq. (43)) of a particular body is determined by conformally mapping the scatterer surface to a new coordinate system by solving Eq. (30), then solving for the scattering coefficients, b_{nm} , for the appropriate boundary condition as specified in the equations of this section.

III. NUMERICAL IMPLEMENTATION

A. General approach

Prediction of the scattering by an axisymmetric finite-length body using the above formulation requires a series of steps involving numerical methods. Given the complexity of the procedure, it is summarized briefly in this section, with some of the challenges elaborated upon in the next section. The shape of the scatterer is first described by the array of points, (r, θ) , in polar coordinates in the xz -plane (Fig. 1). The terms r and θ are then expanded in a Fourier series using Eqs. (21) and (29). The conformal mapping is based upon determining the values of δ_l^c and δ_l^s , which are determined by solving the upper result in the right hand side of Eq. (30). This is a set of nonlinear constraints which are solved in an iterative, numerical manner by an extension of the Newton-Raphson method. The details of the Newton-Raphson method can be found in the Appendix of DiPerna and Stanton (1994) or in many math texts. Once the values of δ_l^c and δ_l^s are determined, the lower result in the right hand side of Eq. (30) is used to determine the mapping coefficients, c_n , which are then used to compute functions, $g(u, w)$ and

$f(u, w)$, of the new coordinate system (Eqs. (26) and (27)). After the values of $g(u, w)$ and $f(u, w)$ are determined, the conformal mapping is complete, and the solution to the Helmholtz equation in the new coordinate system can be determined. The number of terms included in the summations in Eqs. (21), (29) and (30) are chosen in an iterative manner—predictions are made at first with a small number of terms, and then the number is increased for subsequent predictions until the scatterer is accurately mapped to the new coordinate system. The mapping can be verified visually by using $g(u, w)$ and $f(u, w)$ to plot on top of the shape in the original coordinate system (Fig. 1). For some shapes, the conformal mapping method can be avoided by using a function to describe the boundary. In the case of a smooth prolate spheroid, the functions $f = a \sin(w)$ and $g = b \cos(w)$ can be used in Eqs. (26) and (27), where a and b are the semi-minor and semi-major axes of the prolate spheroid, respectively. In the new coordinate system, the external far-field pressure (Eq. (40)) is solved by use of Eqs. (36) - (38). For soft boundary conditions, solve Eq. (54) by numerical integration of Eqs. (52) and (53). The numerical integration can be performed by use of one of numerous integration techniques, many of which are described in Press *et al.*, (1992). In this work, simple matrix summation was used. Likewise for rigid and fluid boundary conditions, solve Eqs. (71) and (80) by performing the numerical integrations in Eqs. (69) and (76) - (77), respectively. With the scattered field coefficients, b_{nm} , the scattering amplitude is finally computed ⁱⁿ Eq. (43). The point at which the summations in Eq. (43) are truncated is determined in an iterative manner. The issues and challenges involved in truncation and performing the matrix inversions in Eqs. (54), (71) and (80) are discussed in the next section.

B. Numerical issues

In general, there exist significant inherent difficulties in the numerical implementation of infinite series solutions. For series solutions for simple geometries such as a sphere or cylinder, and with currently available computers, the series converges relatively rapidly. However, as the shape deviates from a simple geometry, higher modes are required for a converged solution. The problem is particularly complicated for objects of high aspect ratio and irregularity (roughness) on the boundary. The accuracy of the solution must be balanced with accounting for the degree of roughness and elongation of the boundary.

1. Precision

Some of the difficulty in the numerical calculation of the wave functions is merely the time required for the computer to compute the wave functions. Beyond this issue of time, the limiting factors in the numerical implementation are machine precision and matrix manipulation.

The FMM generates a transition matrix, much like the T-matrix model (Waterman, 1968), that relates the incident field coefficients to the scattered field coefficients. For a spherical scatterer, the transition matrix is diagonal and each non-zero term on the main diagonal is an eigenvalue for each mode computed. If the scatterer shape deviates from spherical, the matrix contains off-diagonal terms. The additional higher modal terms required to represent the scattering become extremely small, sometimes falling below the value that can be accurately represented numerically, resulting in a singular matrix in which the true values of its elements are below the precision of the machine. Thus, machine roundoff error is introduced into the solution and quickly dominates the results as it propagates through the solution via repetitive matrix manipulation.

The fundamental problem is finite machine precision. The number of modes required to accurately represent the scattering involves matrix elements that are sometimes numerically smaller than the machine can accurately compute. Little can be done to improve precision since it is a hardware limitation. Future technology may afford greater precision, but the extent to which it improves the solution is difficult to estimate. The relationship between greater precision and increased accuracy in the solution is not necessarily linear, but could be a rapidly decaying one instead.

Besides hardware limitations, numerical accuracy is very dependent upon accurate and efficient numerical implementation of the theory. There are a number of numerical algorithms that improve matrix manipulation and handling of roundoff error that have been investigated in this work, including orthogonal triangular decomposition, LU factorization, balancing of matrices and scaling strategies (Press *et al.*, 1992). The single most important algorithm investigated and used in the implementation of this formulation is the well-known singular value decomposition (SVD) algorithm (Press *et al.*, 1992).

For an ill-conditioned matrix in which some elements are below machine precision, the SVD algorithm sets those numerically indiscernible elements to zero. Eliminating one or more linear combinations of the set of equations that is to be solved is justified because those subspaces are dominated by roundoff error and contribute negligible energy to the solution and contribute principally to error; indeed, the error can be amplified. Singular values whose ratio to the largest singular value is less than N times the machine precision are set to zero (Press *et al.*, 1992). This threshold value is equivalent to the rank of the matrix, which is an estimate of the number of linearly independent rows or columns of a matrix. Eliminating erroneous subspaces

yields a more stable numerical result and a convergent solution at higher frequencies; however, a disadvantage of the method is the potential of removing some energy that contributes to the solution, thereby diminishing the amplitude and structure of the results at higher frequencies. Therefore, the threshold used for SVD must be set with care.

2. Truncation

Regardless of whether the wave functions are difficult to compute and are susceptible to limitations of machine precision, numerical computation of an infinite series such as in Eqs. (40) and (43), cannot be performed exactly due to the fact that there are an infinite number of terms. Furthermore, the point at which the series must be truncated is not necessarily obvious. For lower frequencies and smooth spherical or smooth low-aspect-ratio spheroids (i.e., low eccentricity), reaching a converged solution before the onset of singularity is typically not a problem using currently available personal computers. As the frequency, aspect ratios or degree of irregularity are increased, roundoff error begins to increase as a factor in preventing the solution from being converged.

Given the importance of these numerical issues, a study was conducted to explore the conditions under which the solution would be reliable once numerically evaluated. The "performance envelope" of the FMM for broadside backscattering by smooth prolate spheroids of varying aspect ratios for soft and rigid boundary conditions was investigated (Figs. 2 and 3).

In this study, a "converged" solution is defined as one in which the computation of additional modes does not significantly change the result for a given value of ka . Specifically, the scattering amplitude for a converged solution (although strictly a truncated form of the exact solution) changed by less than 0.1% (an amount chosen arbitrarily in this study) with the com-

putation of additional modes, which correlated very well with visual inspection. "Truncated" and "numerically stable" approximations are less objective and are a relative indication of the degree of reliability. Truncated approximations, as defined in this paper, employ a sufficient number of modes to represent the scattering to a lesser degree of accuracy than the above-defined converged solution, but still generally predicts the overall scattering levels and finer structure. Numerically stable approximations use a sufficient number of modes to adequately represent the overall amplitude, if not the finer structure, of the majority of the scattering. For both the soft (Fig. 2) and rigid (Fig. 3) cases, the solution was obtained for prolate spheroids with aspect ratios ranging from 1:1 (i.e., a sphere) to 13:1, and ka ranging from 0 to 10. Note that a is the semi-minor axis of the prolate spheroid, b is the semi-major axis, and the aspect ratio is b/a . This assignment of notation (a and b) differs from that in some literature, as a in this paper is intended to correspond to a cylindrical radius for the elongated bodies. For each of the two boundary conditions, a converged solution is reached for the sphere and 2:1 aspect ratio prolate spheroid for values of ka up to 10. As the aspect ratio is increased beyond 2:1, the value of ka at which the solution is converged falls off rapidly down to levels of 1.3 (soft) and 1.2 (rigid) at an aspect ratio of 13:1. The truncated approximation and numerically stable approximation behave less predictably as a function of ka and aspect ratio, but indicate generally decreasing convergence values of ka with increasing aspect ratio. The value of ka at which a converged solution is reached in the soft case is generally higher than that of the rigid case, particularly for aspect ratios of 8:1 or less. This is consistent with the fact that the soft case does not include an expression for the derivative of pressure as in the rigid case (Eq. (66)), thus requiring fewer matrix manipulations that would propagate roundoff error.

IV. NUMERICAL RESULTS

All of the results plotted in Sec. IV were generated using Eqs. (43)-(46), (54), (71) and (80) to illustrate predictions as well as demonstrate the accuracy of the FMM in a wide variety of applications. Predictions using the FMM are first compared to those using the exact solution for soft, rigid and fluid spheres. Predictions are then compared between the FMM and various formulations for smooth prolate spheroids for a variety of aspect ratios, frequencies, and incidence and scattering angles. Thirdly, computations are presented for scattering from a realistic, irregular body. Lastly, predictions are presented for scattering by gaseous smooth prolate spheroids in the region of resonance for various aspect ratios.

A. Spheres: comparison with exact solution

Computing the scattering from the sphere is an essential benchmark for the FMM since the exact solutions exist. The results for the soft, rigid and fluid spheres produced by the FMM are identical to the exact solutions (Anderson, 1950) in all three cases (Fig. 4). In the case of fluid boundary conditions, material properties for a weak scatterer (i.e., one having properties resembling that of the surrounding fluid) were used. The specific values were chosen to resemble zooplankton tissue.

B. Prolate spheroids: comparison with various solutions

As mentioned earlier, accurately computing the scattering from a prolate spheroid is a difficult task, particularly at high aspect ratios and high frequencies. Every scattering model has its strengths and weaknesses, so to thoroughly test the scope of applicability for the FMM, it is compared to a variety of models within their ranges of performance. The approaches used

for comparison are the Deformed Finite Cylinder (DFC) model, the T-matrix formulation, the Boundary Element Method (BEM), the exact prolate spheroidal solution and the Kirchhoff approximation.

1. Deformed finite cylinder model (DFC)

Stanton adapted his formulation for the finite cylinder (Stanton, 1988a, b) to finite cylinders of deformation; e.g., prolate spheroids and uniformly bent finite cylinders (Stanton, 1989). The model, which is based on the modal series solution for an infinitely long cylinder, has proven to be accurate at broadside and near-broadside orientations to the prolate spheroid for aspect ratios of 5:1 and higher (Partridge and Smith, 1995). The FMM compares well to the DFC for the case of broadside backscatter from a rigid prolate spheroid of aspect ratios 2:1, 5:1 and 10:1 (Fig. 5). As the aspect ratio is increased, results for the FMM are limited to lower frequencies to maintain a converged solution. In the Rayleigh region ($ka \leq 1$), the TS increases as expected, proportional to $(ka)^4$. Note also that the agreement between the FMM and the DFC in the Rayleigh region improves as the aspect ratio increases, reflecting the fact that the accuracy of the DFC improves with aspect ratio, eventually coinciding with the FMM results.

2. T-matrix method

The T-matrix method is a formally exact, numerical solution that has been the focus of much research to date and has proven to be an accurate model for numerous scattering problems. In two earlier studies, the T-matrix approach has been applied to backscatter and bistatic scattering by rigid prolate spheroids with an aspect ratio of 2:1 (Varadan *et al.*, 1982) and 10:1 (Hackman, 1993) and will be compared with FMM predictions. There is excellent agreement between the

FMM and the T-matrix method in the cases of backscatter for a 2:1 aspect ratio prolate spheroid at broadside ($\theta_0 = 90^\circ$) and oblique ($\theta_0 = 45^\circ$) angles of incidence, as well as in the bistatic geometry of broadside incidence ($\theta_0 = 90^\circ$) and end-on reception ($\theta_r = 0^\circ$) (Fig. 6). There is also excellent agreement between the T-matrix and the FMM after increasing the aspect ratio from 2:1 to 10:1 for the rigid prolate spheroid in the case of broadside and end-on backscatter (Fig. 7). All of the cases in Figs. 6 and 7 illustrate the interference between the specular reflection and a Franz, or creeping wave, and the associated shifts in the peaks and nulls for the different angles of incidence and reception (Uberall *et al.*, 1966).

3. Boundary element method (BEM)

Francis (1993) developed a numerical method of computing the scattering by a finite body using a boundary element method based on a partial application of a Helmholtz gradient formulation. The FMM and BEM agree perfectly to high frequencies ($ka = 10$) in the case of end-on backscatter for a 2:1 aspect ratio rigid prolate spheroid (Fig. 8).

4. Exact prolate spheroidal solution

The exact solution for a prolate spheroid in prolate spheroidal coordinates has been used by various investigators (Yeh, 1967; Furusawa, 1988; and Ye *et al.*, 1997). While this is formally an exact solution, it encounters the same numerical challenges mentioned in Sec. III. Comparisons of the FMM to the exact solution in the case of backscatter and forward scatter for a range of incidence angles ($\theta_0 = 30^\circ, 70^\circ, 90^\circ$) demonstrate good to excellent agreement in all cases (Fig. 9).

5. Kirchhoff approximation

The Kirchhoff approximation is a frequently used approximation for backscattering; however, it is generally limited to the geometric scattering region ($ka >> 1$), perfectly reflecting boundary conditions (soft and rigid) and near-broadside incidence (Born and Wolf, 1999). It is a convenient approximation for the amplitude of the backscatter, but does not accurately represent the oscillations in the amplitude due to the interaction between the specular reflections and Franz waves. Comparisons of the FMM to this approximation within the range of reliability of the Kirchhoff approximation further establish the consistency of the FMM. Specifically, the reduced target strengths for broadside backscattering generally agree well for the single frequencies presented, with improved agreement as the frequency increases (Fig. 10). At $ka = 1$, the Kirchhoff approximation is near the limit of its range of validity and under-estimates the amplitude. Additionally, it can be seen that the Kirchhoff approximation falls off much more rapidly than the FMM for all ka as the incidence angle moves away from broadside.

C. Irregular bodies: comparison with Kirchhoff approximation

As emphasized earlier, accurate computation of the scattering by smooth elongated bodies is not a simple task, particularly as the aspect ratio and frequencies increase. The additional complexity of an irregular surface further complicates an already difficult problem. A key distinction of the FMM is its ability to conformally map an irregular axisymmetric surface to an orthogonal coordinate system that better fits the scatterer surface. To demonstrate the practical application of the FMM to a realistic, asymmetrical, irregular body with non-Gaussian roughness, the acoustic scattering by a gas-filled swimbladder from an alewife fish (*Alosa pseudoharengus*) has been modeled and compared with the Kirchhoff approximation for two representative shapes

corresponding to the dorsal and ventral aspects of the swimbladder (Figs. 11 and 12). This particular problem was chosen as fish are a significant scatterer of sound in the ocean, and the swimbladder is the organ in the fish that generally dominates the scattering. A more extensive treatment of this application is given in Reeder *et al.* (submitted). At these values of ka , soft boundary conditions were used, given the high contrast in material properties between the gas and surrounding tissue. There is generally reasonable agreement between FMM and Kirchhoff for most values of ka for Shape #1 in Fig. 11, but for Shape #2 in Fig. 12, the Kirchhoff predictions generally under-estimate the scattering relative to the FMM at angles well off broadside.

D. Low ka resonance scattering for gaseous bodies: comparison with T-matrix and exact prolate spheroidal solutions

In contrast to the cases of rigid and weakly-scattering objects described above whose scattering levels decrease dramatically in the $ka \ll 1$ region, gaseous bodies have a strong resonance in that region and have been the subject of many earlier studies. Although in the low ka region there are fewer restrictions in the calculations, challenges still remain in the prediction of scattering from gaseous bodies with high aspect ratios. In this study, the FMM is directly compared with the T-matrix method and the exact prolate spheroidal solution over a range of aspect ratios up to 20:1 for constant volume prolate spheroids. Predictions from the T-matrix method and FMM are compared in Fig. 13 for aspect ratios up to 16:1; however, results for aspect ratios up to 20:1 were presented by Feuillade and Werby (1994) using the T-matrix method, as well as Ye and Hoskinson (1998) using the exact prolate spheroidal solution. In addition, low ka resonance scattering by gaseous bodies of higher aspect ratio (up to 100:1) was calculated with no difficulties relative to the numerical issues cited earlier. These ratios are much higher than what

has previously appeared in the literature (Strasberg, 1953; Weston, 1967; Feuillade and Werby, 1994; Ye and Hoskinson, 1998). The FMM accurately predicts the scattering in the resonance region—the increase in the resonance frequency, the decrease in the resonance amplitude and the broadening of the resonance peaks for prolate spheroids of constant volume and increasing aspect ratio within the verifiable range of aspect ratios presented in the literature (up to 20:1 aspect ratios).

V. SUMMARY AND CONCLUSIONS

An extension of a two-dimensional conformal mapping approach to scattering by irregular, finite-length bodies of revolution has been presented for three boundary conditions. The model conformally maps the coordinate variables of the original coordinate system to a new orthogonal coordinate system in which the locus of all points where the new radial coordinate is a constant exactly coincides with the scatterer surface. The solutions to the transformed Helmholtz equation are a general solution for the total pressure in the case of far-field scattering from a finite body of revolution. This model has been shown to be very accurate in the prediction of scattering from smooth, symmetric bodies for a wide range of frequencies (Rayleigh through geometric scattering region), scattering angles (monostatic and bistatic), aspect ratios and boundary conditions, and for all angles. Reasonable agreement has also been demonstrated for irregular, realistic shapes when compared to the Kirchhoff approximation. This work represents a significant advancement by providing a numerically efficient formulation that is applicable over a wide range of frequencies, scattering angles and geometries for soft, rigid and fluid boundary conditions.

There is great potential for further development of this model, including application to acous-

tic scattering by elastic solids and shells. The implementation of better numerical integration techniques, the use of extended precision format of floating point arithmetic or various smoothing techniques (Yamashita, 1990) could delay the onset of ill-conditioned matrices, accelerating convergence. New scaling techniques based upon the physical scattering mechanisms could also increase accuracy (Schmidt, 1993).

ACKNOWLEDGMENTS

The authors would like to thank Dr. Daniel T. DiPerna (*Signatures Directorate, Naval Surface Warfare Center, Carderock Division, Bethesda, Maryland*) who derived an early form of the general solution and provided much guidance during the course of this work. The authors would also like to thank Dr. Trevor Francis of the University of Birmingham, UK, for generously providing the BEM calculation for Fig. 8. This work was supported by the U.S. Navy, the U.S. Office of Naval Research, and the Massachusetts Institute of Technology/Woods Hole Oceanographic Institution Joint Program in Oceanographic Engineering. This is Woods Hole Oceanographic Institution contribution number 10701.

REFERENCES

Anderson, V.C. (1950) "Sound scattering from a fluid sphere," *J. Acoust. Soc. Am.*, 22:426-431.

Born, M., and Wolf, E. (1999) *Principles of Optics* (Seventh Edition, University Press, Cambridge).

Bowman, J.J., Senior, T.B.A., and Uslenghi, P.L.E. (1987) *Electromagnetic and Acoustic Scattering by Simple Shapes* (Hemisphere Publishing Corp., New York).

Clay, C.S., and Horne, J.K. (1994) "Acoustic models of fish: The Atlantic cod (*Gadus morhua*)," *J. Acoust. Soc. Am.*, 96:1661-1668.

DiPerna, D.T., and Stanton, T.K. (1994) "Sound scattering by cylinders of noncircular cross section: A conformal mapping approach," *J. Acoust. Soc. Am.*, 96:3064-3079.

Feuillade, C., and Werby, M.F. (1994) "Resonances of deformed gas bubbles in liquids," *J. Acoust. Soc. Am.*, 96:3684-3692.

Flammer, C. (1957) *Spheroidal Wave Functions* (Stanford University Press, Stanford).

Francis, D.T.I. (1993) "A gradient formulation of the Helmholtz integral equation for acoustic radiation and scattering," *J. Acoust. Soc. Am.*, 93:1700-1709.

Francis, D.T.I. (2001) Personal communication.

Furusawa, M. (1988) "Prolate spheroidal models for predicting general trends of fish target strength," *J. Acoust. Soc. Jpn. (E)*, 9:13-24.

Gaunaurd, G.C. (1985) "Sonar cross sections of bodies partially insonified by finite sound beams," *IEEE J. Ocean. Eng.*, 10:213-230.

Hackman, R.H. (1993) "Underwater Scattering and Radiation," In *Physical Acoustics*, Vol. XXII, Ed. A.D. Pierce and R.N. Thurston (Academic Press, San Diego).

Hackman, R.H., and Todoroff, D.G. (1985) "An application of the spheroidal-coordinate-based transition matrix: The acoustic scattering from high aspect ratio solids," *J. Acoust. Soc. Am.*, 78:1058-1071.

Hildebrand, F.B. (1964) *Advanced Calculus for Applications* (Prentice-Hall, New Jersey).

Lakhtakia, A., Varadan, V.K., and Varadan, V.V. (1984) "Iterative extended boundary condition method for scattering by objects of high aspect ratios," *J. Acoust. Soc. Am.*, 76:906-912.

Levy, B.R., and Keller, J.B. (1959) "Diffraction by a smooth object," *Comm. on Pure Applied Math.*, 12:159-209.

Morse, P.M., and Feshbach, H. (1953) *Methods of Theoretical Physics* (McGraw-Hill, Boston).

Partridge, C. and Smith, E.R. (1995) "Acoustic scattering from bodies: Range of validity of the deformed cylinder method," *J. Acoust. Soc. Am.*, 97:784-795.

Press, W.H., Teukolsky, S.A., Vetterling, W.T. and Flannery, B.P. (1992) *Numerical Recipes in Fortran: The Art of Scientific Computing* (Second Edition, Cambridge University Press, Australia).

Rayleigh, Lord (J.H. Strutt) (1945) *The Theory of Sound* (Dover, New York).

Reeder, D.B., Jech, J.M., and Stanton, T.K. (submitted) "Broadband acoustic backscatter and high resolution morphology of fish: Measurement and modeling," *J. Acoust. Soc. Am.*

Schmidt, H. (1993) "Numerically stable global matrix approach to radiation and scattering from spherically stratified shells," *J. Acoust. Soc. Am.*, 94:2420-2430.

Stanton, T.K. (1988a) "Sound scattering by cylinders of finite length. I. Fluid cylinders," *J. Acoust. Soc. Am.*, 83:55-63.

Stanton, T.K. (1988b) "Sound scattering by cylinders of finite length. II. Elastic cylinders," *J. Acoust. Soc. Am.*, 83:64-67.

Stanton, T.K. (1989) "Sound scattering by cylinders of finite length. III. Deformed cylinders," *J. Acoust. Soc. Am.*, 86:691-705.

Strang, G. (1986) *Introduction to Applied Mathematics* (Wellesley-Cambridge, Wellesley, MA).

Strasberg, M. (1953) "The pulsation frequency of nonspherical gas bubbles in liquids," *J. Acoust. Soc. Am.*, 25:536-537.

Tobacman, W. (1984) "Calculation of acoustic wave scattering by means of the Helmholtz integral equation," *J. Acoust. Soc. Am.*, 76:599-607.

Uberall, H., Doolittle, R.D., and McNicholas, J.V. (1966) "Use of sound pulses for a study of circumferential waves," *J. Acoust. Soc. Am.*, 39:564-578.

Urick, R.J. (1983) *Principles of underwater sound* (Peninsula Publishing).

Varadan, V.K., Varadan, V.V., Dragonette, L.R., and Flax, L. (1982) "Computation of rigid body scattering by prolate spheroids using the T-matrix approach," *J. Acoust. Soc. Am.*, 71:22-25.

Waterman, P.C. (1968) "New formulation of acoustic scattering," *J. Acoust. Soc. Am.*, 45:1417-1429.

Weston, D.E. (1967) "Sound propagation in the presence of bladder fish," *Underwater Acoustics*, Ed. by V.M. Albers (Plenum Press, New York).

Yamashita, E. (1990) *Analysis Methods for Electromagnetic Wave Problems* (Artech House, Norwood, MA).

Ye, Z., Hoskinson, E., Ding, L., and Farmer, D.M. (1997) "A method for acoustic scattering by slender bodies. I. Theory and verification," *J. Acoust. Soc. Am.* 102:1964-1976.

Ye, Z. and Hoskinson, E. (1998) "Low-frequency acoustic scattering by gas-filled prolate spheroids in liquids. II. Comparison with the exact solution," *J. Acoust. Soc. Am.*, 103:822-826.

Yeh, C. (1967) "Scattering of acoustic waves by a penetrable prolate spheroid. I. Liquid prolate spheroid," *J. Acoust. Soc. Am.* 42:518-521.

Figure Captions

Fig. 1: Scattering geometry for an irregular, axisymmetric finite-length body. The body is symmetric about the z -axis. The azimuthal angular coordinates, ϕ and ν , range from 0 to 2π in the xy -plane, and the polar angular coordinates, θ and w , range from 0 to π , measured from the z -axis. The radial coordinate in the (u, w, v) coordinate system equals zero on the surface. Broadside incidence corresponds to $\theta = 90$ degrees. End-on incidence corresponds to $\theta = 0$ and 180 degrees. In the new coordinate system, $g(u, w)$ is the length along the z -axis, and $f(u, w)$ is the projection in the xy -plane.

Fig. 2: Performance envelope for broadside backscatter for a smooth prolate spheroid with soft boundary conditions as a function of ka and aspect ratio. A converged solution is defined in this paper as one in which the computation of additional modes changed the scattering amplitude by less than 0.1% for a given value of ka . As the aspect ratio or value of ka is increased, converged solutions are more difficult to obtain. Aspect ratio (AR) is the ratio of length to width of the prolate spheroid (AR=1 for a sphere). The semi-minor axis of the prolate spheroid is designated as a .

Fig. 3: Performance envelope for broadside backscatter by a smooth prolate spheroid with rigid boundary conditions as a function of ka and aspect ratio. Converged solutions are defined in the caption of Fig. 2.

Fig. 4: FMM and exact solutions: Reduced target strength as a function of ka for soft, rigid and fluid spheres. Mass and sound speed contrasts for the (weakly scattering) fluid case are $g=1.043$ and $h=1.052$, respectively. Exact solution calculation based on formulation from Anderson (1950).

Fig. 5: FMM and DFC: Reduced target strength of rigid prolate spheroids at broadside incidence as a function of ka for aspect ratios of 2:1, 5:1 and 10:1. DFC calculations are based on the formulation from Stanton (1989a). The agreement between the FMM and DFC improves as the aspect ratio increases, which is consistent with the fact that the DFC is valid in the limit of high aspect ratio geometries.

Fig. 6: FMM and T-matrix: Magnitude of backscattered and bistatic form function of a 2:1 rigid prolate spheroid as a function of ka for the case of broadside backscatter, backscatter at oblique incidence and bistatic scattering. T-matrix results are from Figs. 3, 4 and 5 of Varadan *et al.* (1982). The form function is given in Eq. (46).

Fig. 7: FMM and T-matrix: Magnitude of backscattered form function for a 10:1 rigid prolate spheroid as a function of ka for the case of broadside incidence and end-on incidence. T-matrix results are from Fig. 37(a) of Hackman (1993). The form function is given in Eq. (46).

Fig. 8: FMM and BEM: Reduced target strength as a function of ka for a 2:1 rigid prolate spheroid at end-on incidence. The agreement continues well past $ka=10$. BEM results are from Francis (2001).

Fig. 9: FMM and exact prolate spheroidal solution: Reduced target strength as a function of ka for a 10:1 rigid prolate spheroid at incidence angles of 30, 70 and 90 degrees for backscatter and forward scatter. Exact prolate spheroidal solutions are from Fig. 7 of Ye *et al.* (1997).

Fig. 10: FMM and Kirchhoff approximation: Reduced target strength as a function of angle for a 5:1 soft prolate spheroid at $ka=1$, $ka=2$ and $ka=3$. Kirchhoff approximation results are based on the formulation from Born and Wolf (1999). The largest differences occur well off broadside, where the Kirchhoff approximation characteristically underpredicts the scattering.

Fig. 11: FMM and Kirchhoff approximation: Target strength as a function of angle for irregular Shape #1 at $ka=1$, $ka=2$, $ka=3$ and $ka=4$. Kirchhoff approximation results are based on the formulation from Clay and Horne (1994). Shape #1 is shown in the bottom frame. The vertical axis is exaggerated to better illustrate the irregularity of the surface. Broadside corresponds to zero degrees.

Fig. 12: FMM and Kirchhoff approximation: Target strength as a function of angle for irregular Shape #2 at $ka=1$, $ka=2$, $ka=3$, $ka=4$ and $ka=5$. Kirchhoff approximation

results are based on formulation from Clay and Horne (1994). Shape #2 is shown in the bottom frame. The vertical axis is exaggerated to better illustrate the irregularity of the surface. Broadside corresponds to zero degrees.

Fig. 13: FMM and T-matrix: Magnitude of normalized backscattering amplitude as a function of ka_e for a gaseous ($g=0.00126$, $h=0.22$) prolate spheroid at broadside incidence. Results from the FMM (top panel) are compared to results from the T-matrix method (bottom panel) from Fig. 4(a) of Feuillade and Werbe (1994). The single dots in the top panel are peak amplitudes for aspect ratios listed in parentheses. The scattering amplitude on the vertical axis is normalized to the peak amplitude of the sphere. As the aspect ratio of the spheroid is increased beyond 1:1, the dimensions of the spheroid are changed to maintain a volume equal to that of the original sphere. Thus, the a_e in ka_e is the equivalent spherical radius of the object, corresponding to the radius of the sphere (the 1:1 case shown) that has the same volume as the prolate spheroid. Results for aspect ratios up to 20:1 were tabulated by Feuillade and Werby (1994) using the T-matrix method, as well as Ye and Hoskinson (1998) using the exact prolate spheroidal solution. There is excellent agreement among predictions from all three formulations for aspect ratios up to 20:1.

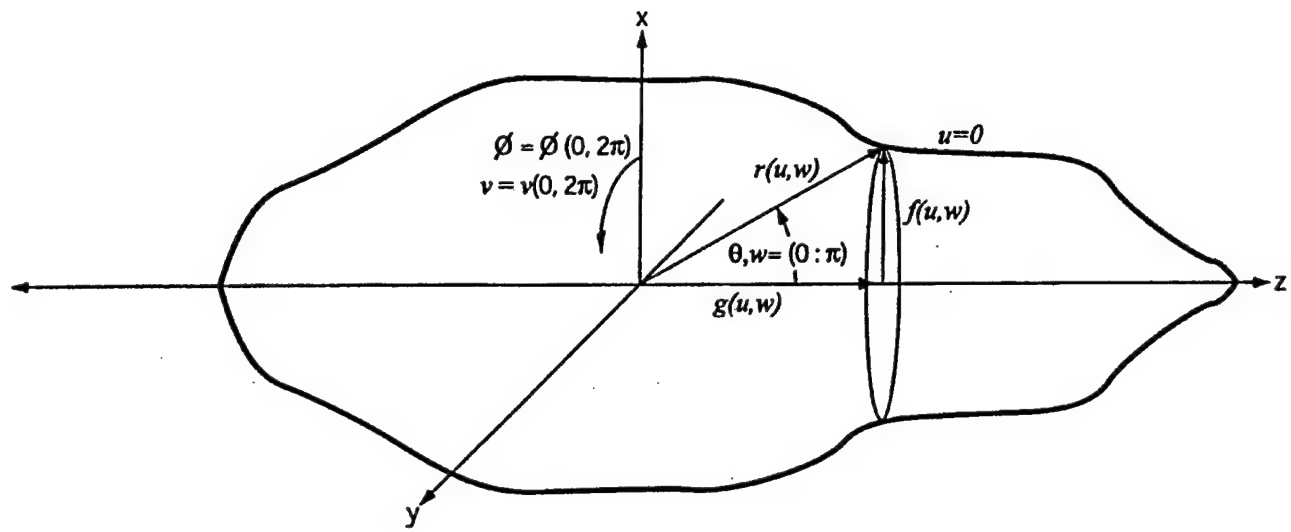


Fig 1

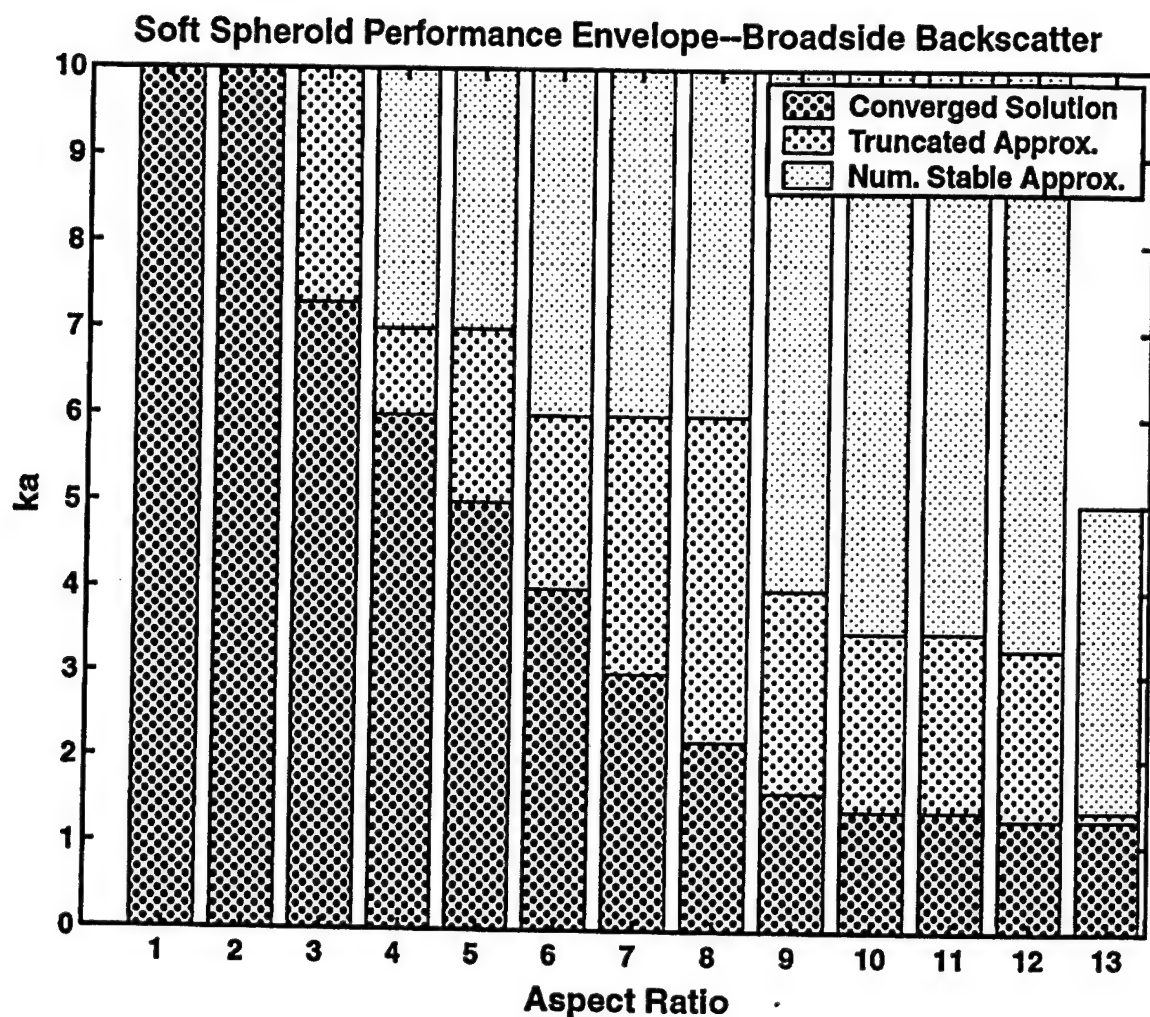


Fig 2

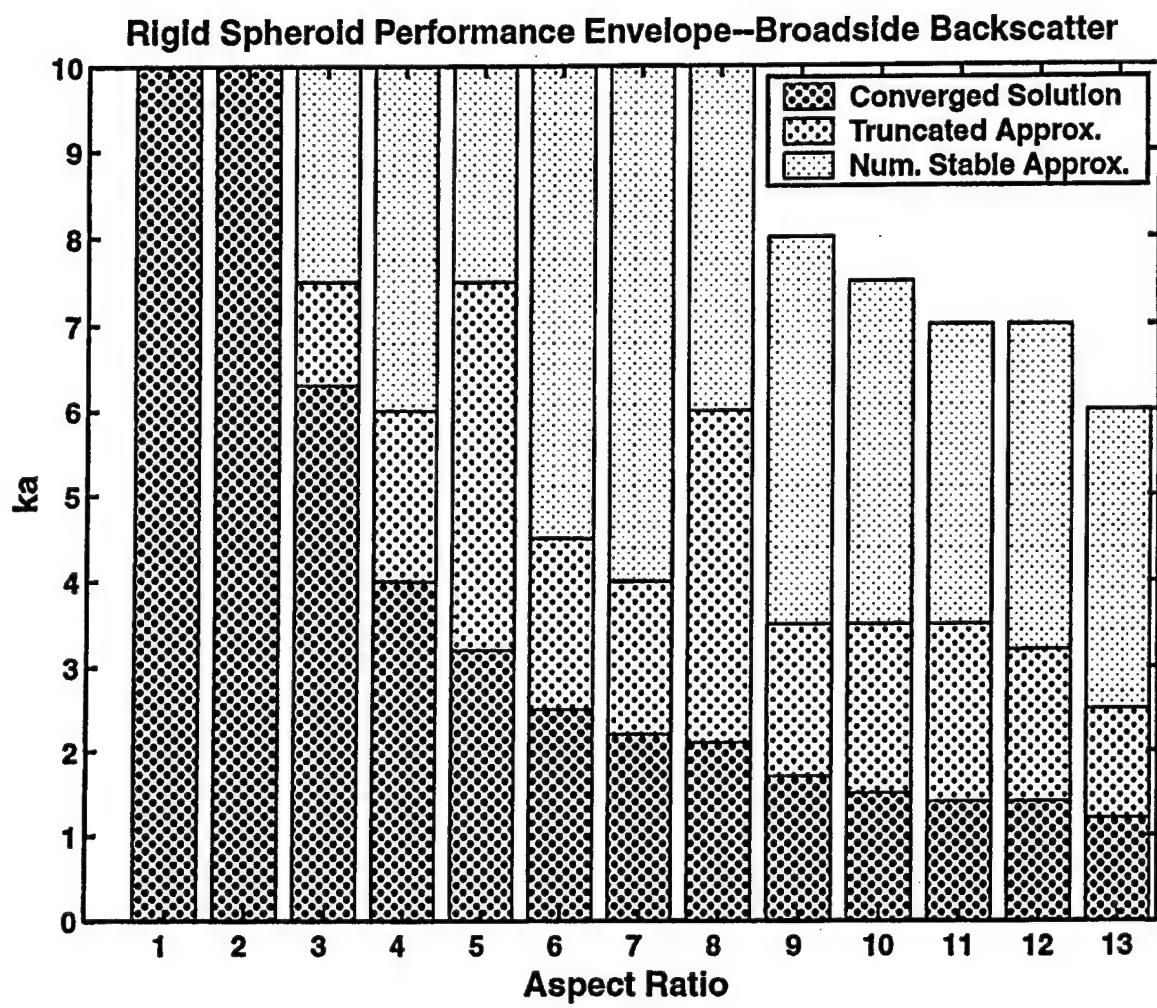
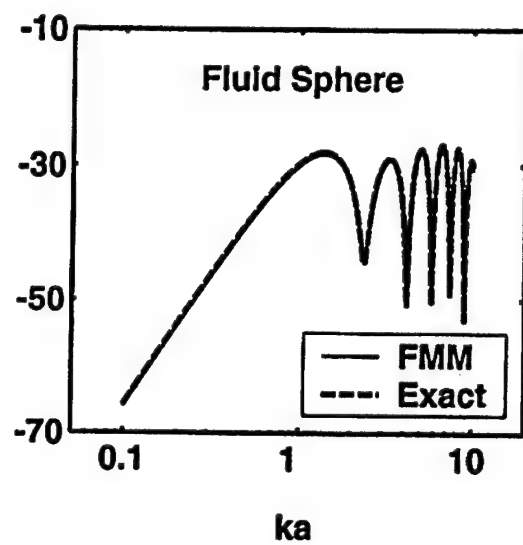
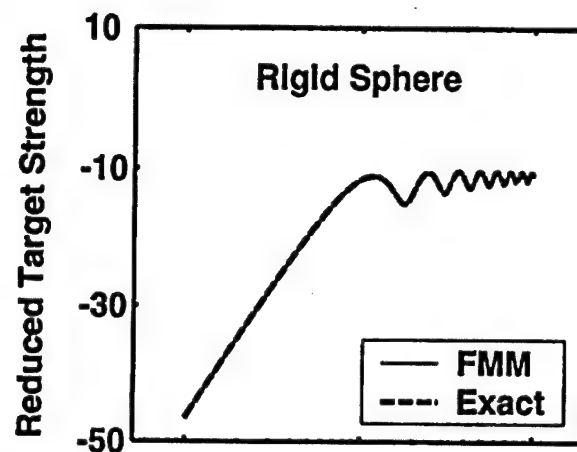
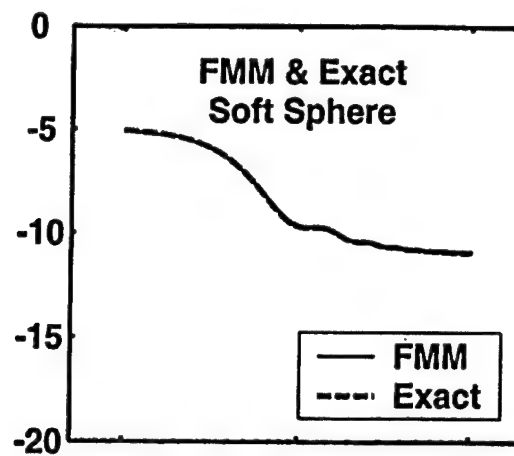


Fig. 3



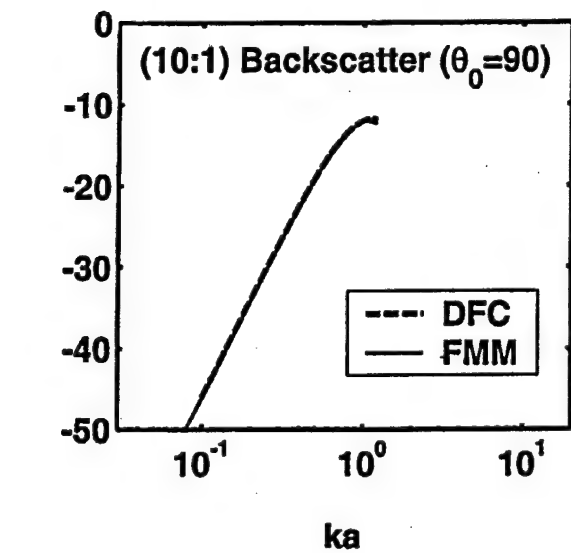
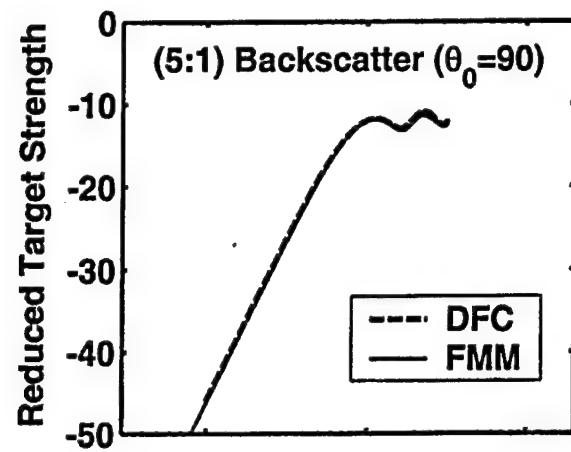
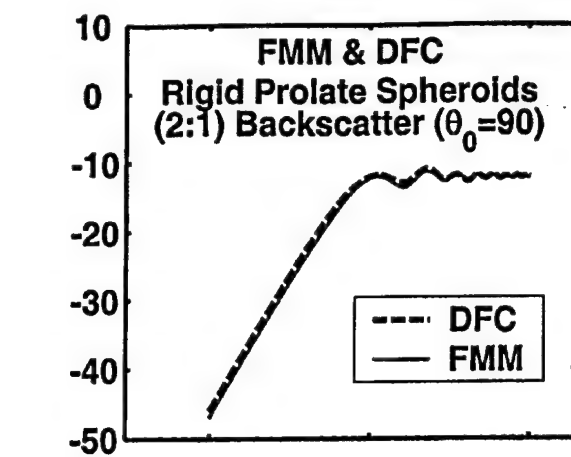


Fig 5

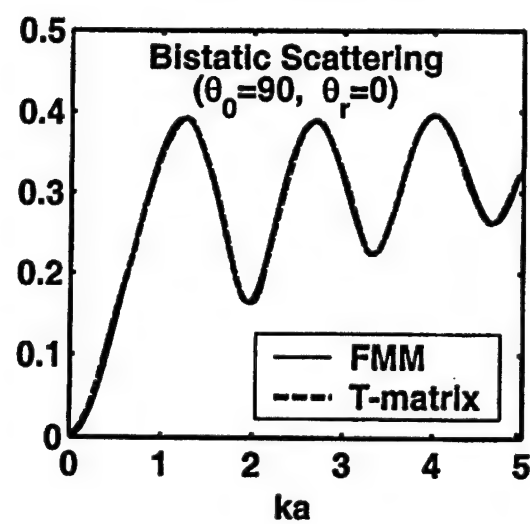
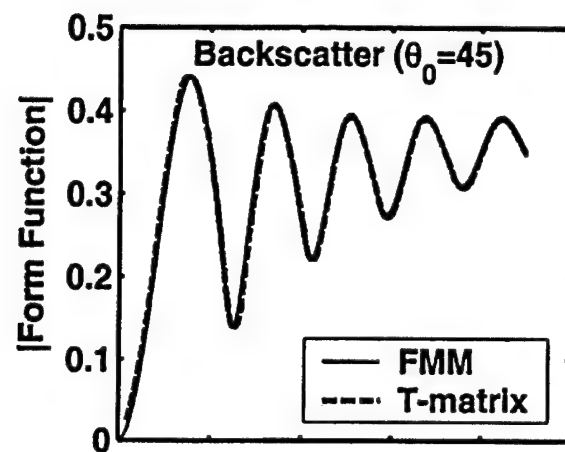
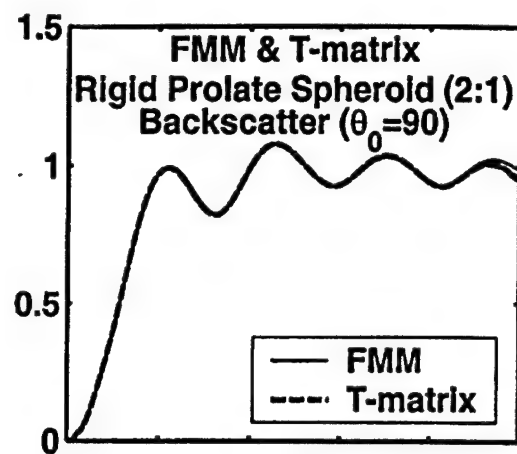


Fig 6

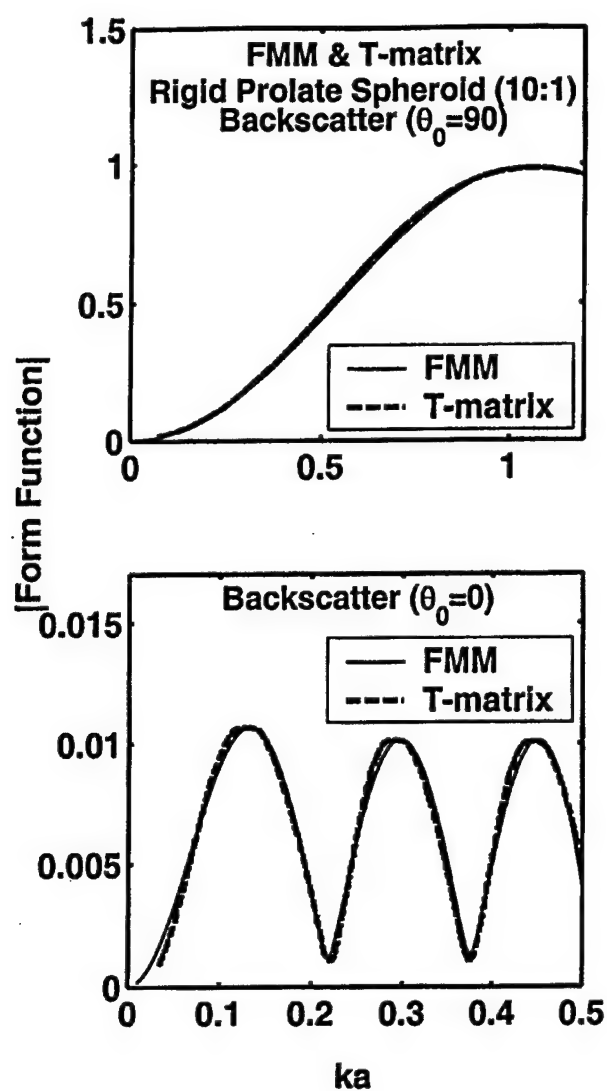


Fig 7

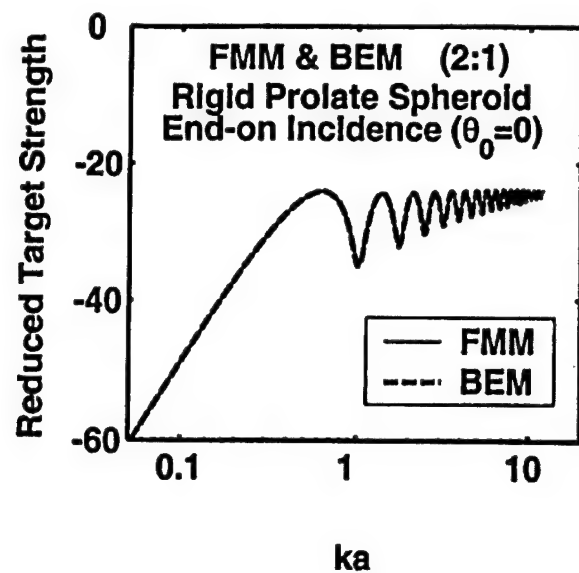


Fig 8

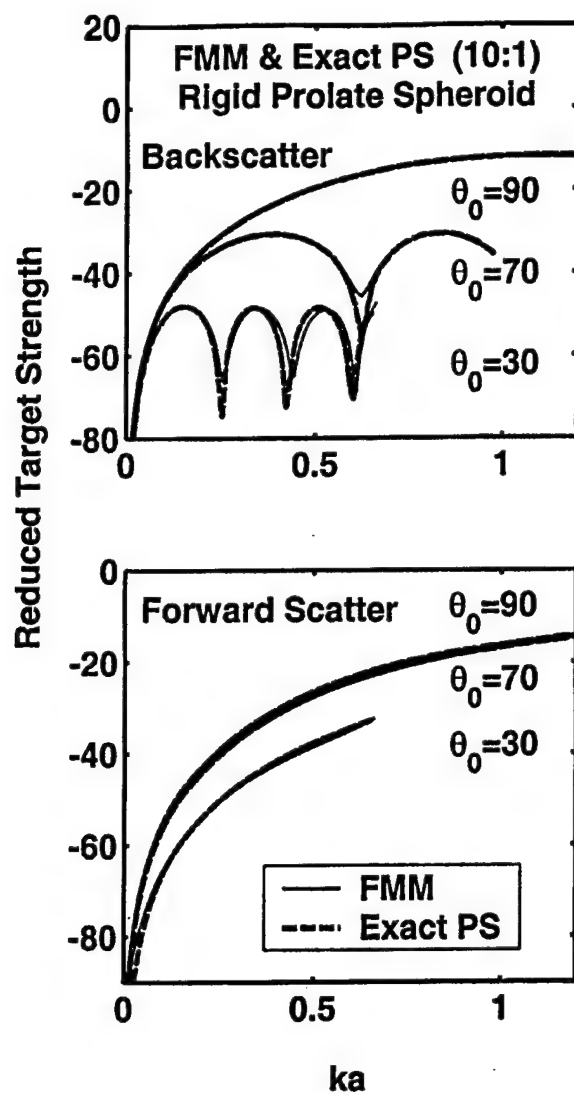
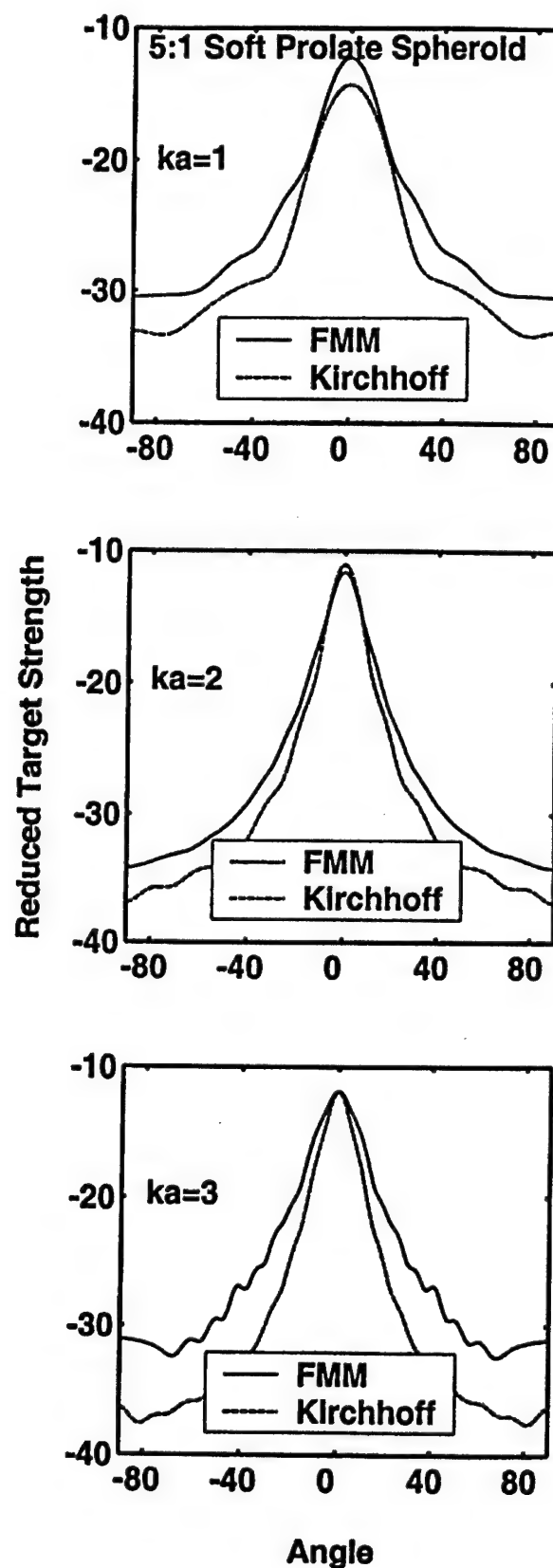


Fig 9



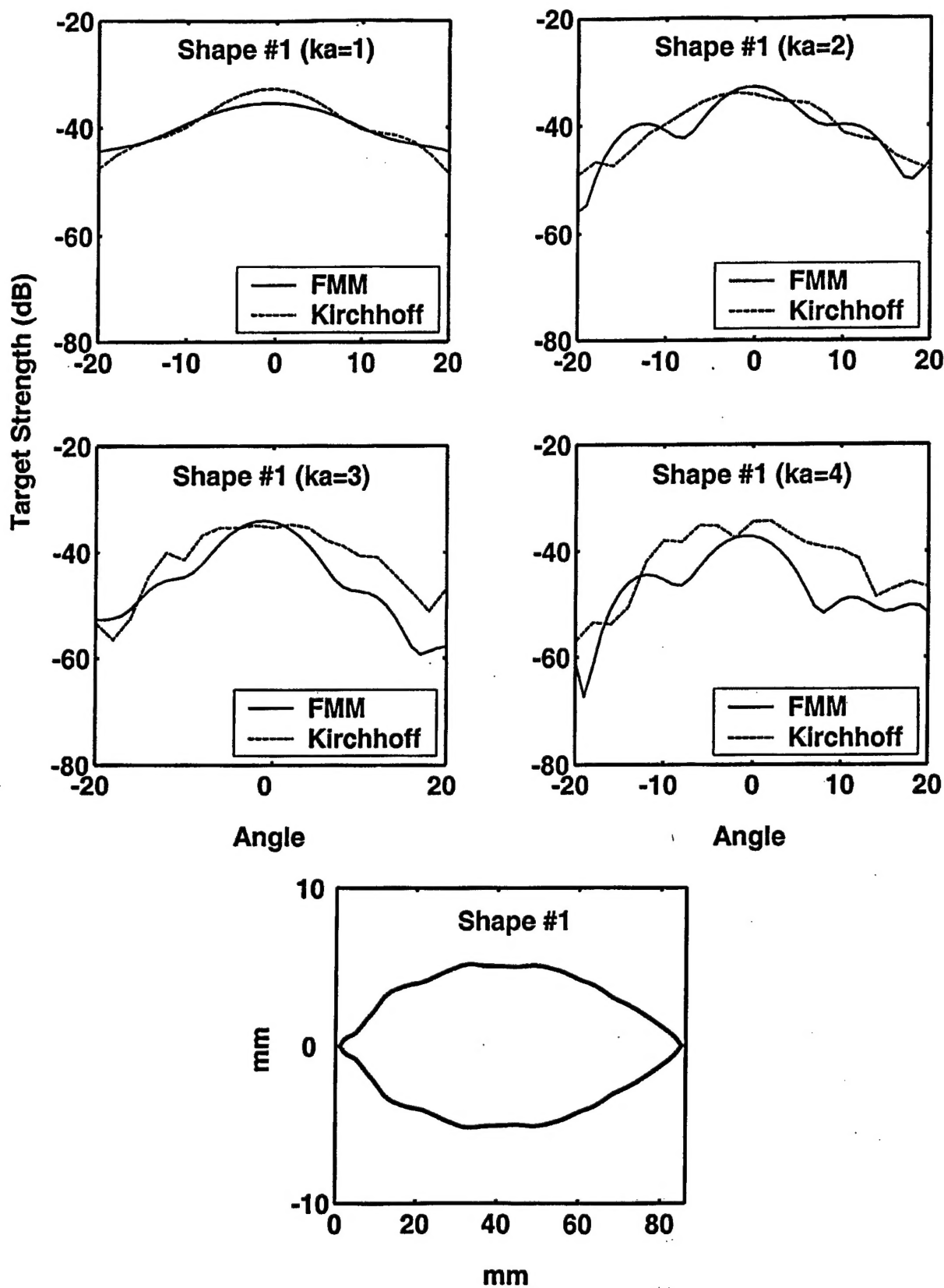


Fig 11

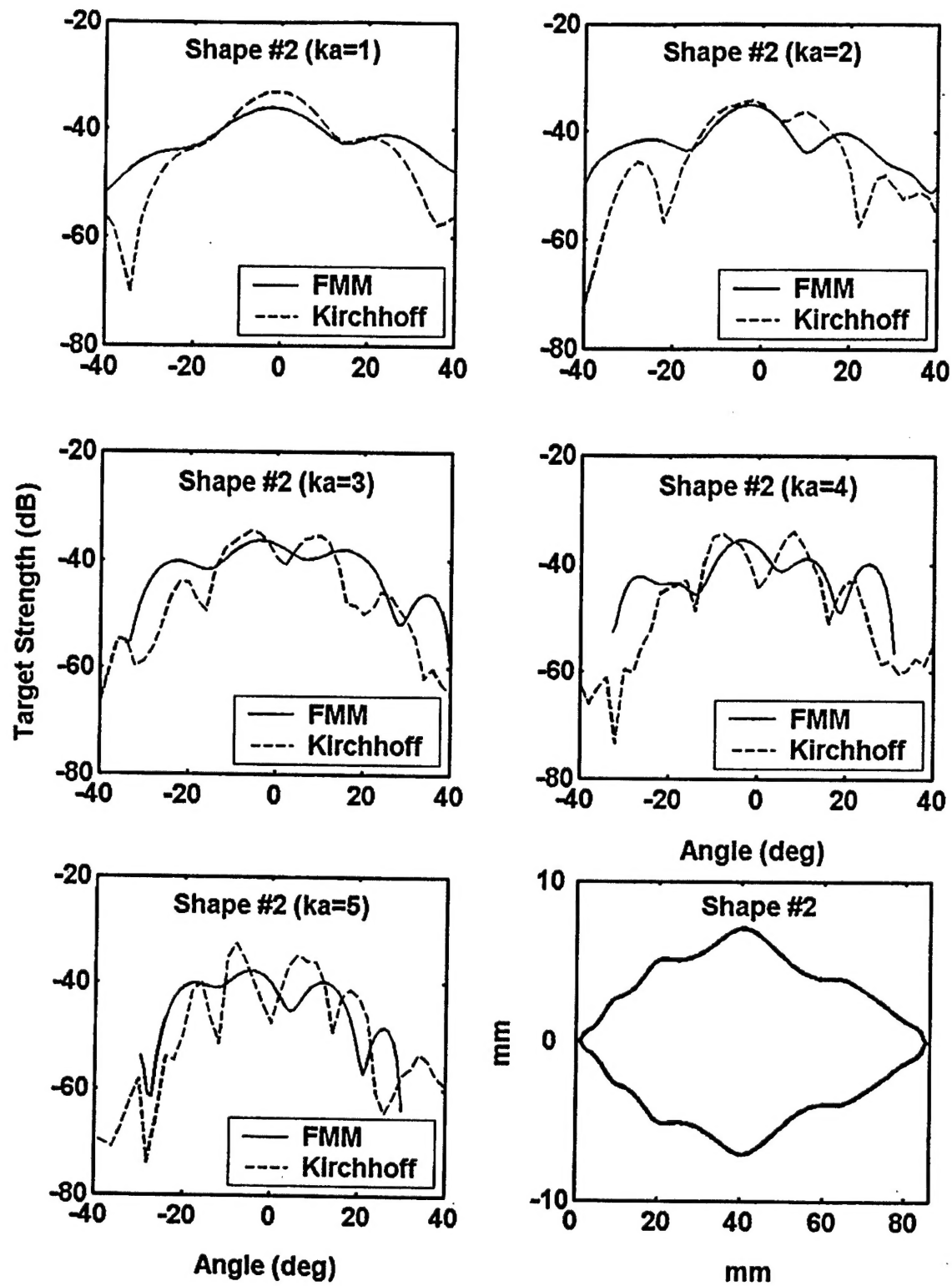


Fig 12

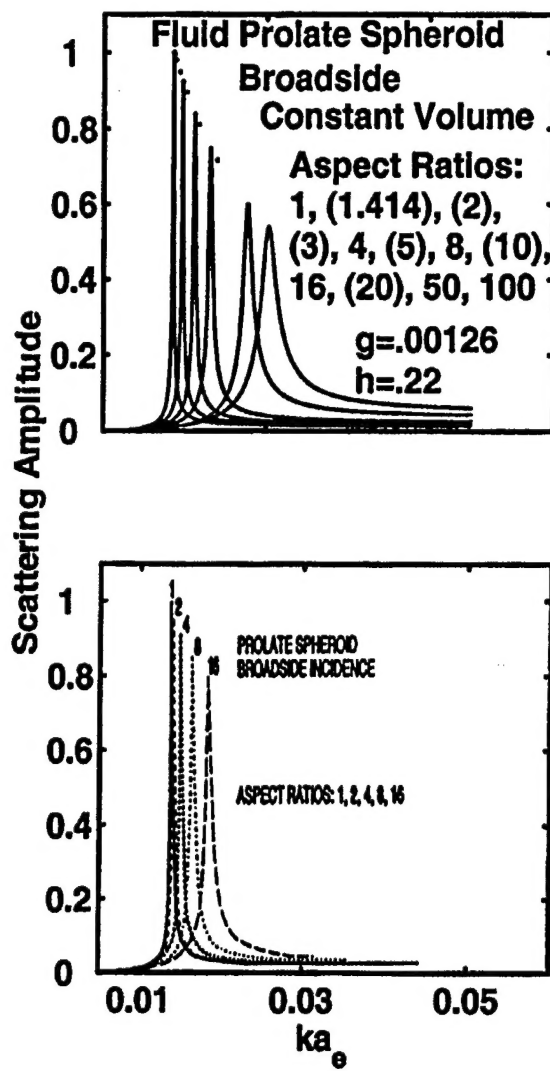


Fig 13

